A Joint Control With Variable ZVS Angles for Dynamic Efficiency Optimization in Wireless Power Transfer System

Yongbin Jiang , *Student Member, IEEE*, Laili Wang , *Senior Member, IEEE*, Jingyang Fang , *Member, IEEE*, Chenxu Zhao, Kangping Wang , *Member, IEEE*, and Yue Wang , *Member, IEEE*

Abstract—Tight voltage regulation and high efficiency are fundamental objectives of wireless power transfer systems (WPTSs) as power supplies. Although the well-established impedance matching control attempts to achieve high efficiency, the associated extra dc–dc converters or hard switching of converters in WPTSs reduce the overall system efficiency, particularly for high-power applications. In this article, under zero voltage switching (ZVS) conditions, the minimum power loss point is derived and proved in detail with different ZVS angles. Moreover, a joint control with variable ZVS angles (JC-VZA) is proposed to ensure ZVS of all switches and achieve the required output, simultaneously. This control scheme is implemented by use of controllers in both sides of WPTSs, which adjust their respective ZVS angles for dynamic efficiency optimization. Under ZVS conditions, the proposed JC-VZA features an optimal amount of reactive power that achieves the minimum total power loss by significantly reducing the switching loss. As a result, the experimental results obtained from our WPTS prototype verify its superiority. With a coupling coefficient k of 0.2 or 0.15, the maximum efficiency reaches 96.8% or 95.0% under the power rating of 288 W (rated load) as well as 92.4% or 88.7% in the case of light load (9% of 288 W).

Index Terms—Dynamic efficiency optimization, joint control with variable ZVS angles (JC-VZA), wireless power transfer system (WPTS), zero voltage switching (ZVS).

I. INTRODUCTION

WIRELESS power transfer (WPT) is an emerging means of power delivery in many applications, such as biomedical implants [1]–[3], consumer electronics [4]–[6], underwater loads [7]–[9], and electric vehicles (EVs) [10]–[13], where physical contact is inconvenient or impossible. Compared with plug-in charging systems, WPT systems (WPTSs) enable electrical and mechanical isolation, minimize the use of cables and sockets, and ensure safe operation under harsh environments.

However, low efficiency acts as one large obstacle that has retarded the widespread adoption of WPTSs. Especially in EV applications, the ever-changing charging voltage and equivalent resistance of battery packs can greatly reduce the transfer efficiency of WPTSs during charging processes [14].

To overcome this shortcoming, the concept of impedance matching control is introduced. It aims to dynamically reshape the equivalent load impedance of battery packs to optimize the system efficiency [15]. As an implementation, two additional dc–dc converters are employed, which allow the regulation of output voltage and impedance matching, simultaneously [4], [15]. Although being effective in terms of control, this method necessitates two auxiliary dc–dc converters that inevitably increase system cost, complexity, and overall power loss.

To get rid of dc–dc converters while ensuring impedance matching, one option lies in the better utilization of an inverter and an active rectifier (AR) [16]–[19]. It can be achieved by adjusting their phase shift angles, known as dual phase shift control (DPSC). With DPSC, the WPTS can optimize the transfer efficiency by selecting their phase shift angles reasonably [16], [17]. Moreover, by DPSC, it is possible to obtain extra desirable features. For example, it is demonstrated that DPSC can reduce the current stresses on both sides of WPTSs [18]. On the basis of DPSC, the power angle of the AR, as an additional control variable, is further introduced to fix the problem of resonant parameter mismatch [19]. However, in the aforementioned WPTSs, the zero-voltage switching (ZVS) of the inverter and the AR cannot be guaranteed. It is worth noting that ZVS is vital for system efficiency improvement and electromagnetic interference (EMI) reduction as it can significantly reduce switching losses, particularly for high-power applications [20]–[24].

An enhanced DPSC is proposed in the dual active bridge (DAB) to achieve ZVS and power regulation with the same

duty cycle of two sides [25]. However, only a special case, i.e., ($nV_{DC2}/V_{DC1} = 1$, n is the turns ratio of the transformer), is investigated and the theoretical analysis lacks universality. In addition, a triple-phase-shift (TPS) control strategy is used in DAB to achieve multiobjective optimization [26], [27]. Moreover, similar to TPS in DAB, an optimal TPS control strategy is also proposed in the WPTSs [22]. It features to adjust the phase shift angle between the ac square waveforms of the inverter and the AR to achieve ZVS. However, this method suffers from implementation issues, as it is very difficult to accurately synchronize driver signals of two separate controllers while it is easy for DAB to implement TPS.

In [23], a phase-shift soft-switching control strategy is proposed to achieve ZVS of the inverter and the AR. Based on DPSC, the authors also make both the inverter and the AR achieve zero ZVS angles to minimize the reactive power and achieve the required output simultaneously. Unfortunately, the authors just analyze a special case that the input dc voltage equals the output dc voltage. However, when the input dc voltage is unequal to the output dc voltage, the phase-shift soft-switching control strategy cannot always achieve the maximum transfer efficiency.

In this article, on the premise of ZVS of all switches, the derivations of minimum power loss conditions are given in detail, which help the WPTS to identify the minimum power loss point under different operating conditions. Moreover, to achieve the required output and ZVS at the same time, a joint control with variable ZVS angles (JC-VZA) is proposed to adjust ZVS angles of the inverter and the AR. Furthermore, by using the JC-VZA with dynamic efficiency optimization method based on "perturb-and-observe" (P&O), the WPTS will easily find out the minimum power loss point to achieve the maximum transfer efficiency. Compared with the traditional DPSC [16]–[19], although some reactive power is introduced by using the proposed JC-VZA, it can maximize the system transfer efficiency under ZVS conditions.

The remainder of this article is organized as follows. Section II presents the basic operating principles of the WPTS and derives the transfer power equations. Section III presents ZVS conditions and some features on the boundary curves. Section IV identifies the minimum power loss point and gives detailed proofs. Section V introduces the JC-VZA with dynamic efficiency optimization method. The experimental results are given in Section VI. Finally, Section VII concludes this article.

II. BASIC ANALYSIS OF WPTS WITH AR

A. Equivalent Circuit Analysis

The schematic of a series-series type (SS-type) WPTS with an AR is shown in Fig. 1(a). The topology of the WPTS is composed of a high-frequency full-bridge inverter, an SS-type resonant network, and a high-frequency full-bridge AR. The inverter contains four switches ($S_1 \sim S_4$), which operates in the complementary mode and converts a dc voltage V_1 into a high-frequency ac voltage v_{ab}. The primary coil L_1 and its resonant capacitor C_1 are in series and stimulated by v_{ab}, and the high-frequency alternating magnetic field is generated
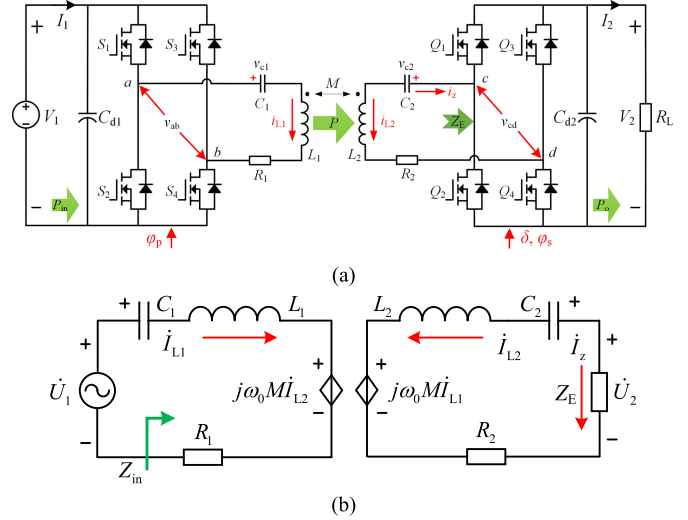

Fig. 1. (a) Schematic of a SS-type WPTS. (b) Its ac equivalent circuit.

by L_1 consequently. According to the law of electromagnetic induction, a voltage is induced in the secondary coil L_2, and powers the load R_L with an output dc voltage V_2 through a serial resonant capacitor C_2 and a full-bridge AR.

Generally speaking, the fundamental harmonic model is commonly used to analyze the WPTS, which is depicted in Fig. 1(b). U_1 and U_2 represent the rms values of fundamental components of v_{ab} and v_{cd}, respectively. I_{L1} and I_{L2} represent the rms values of primary and secondary resonant currents, respectively. R_1 and R_2 stand for the equivalent series resistors (ESRs) of resonant networks of primary and secondary sides, respectively. L_1 and L_2 are the self-inductances of primary and secondary coils, respectively. M is the mutual inductance and the coupling coefficient k of coils satisfies $k = M / \sqrt{L_1 L_2}$. Z_E is the input ac equivalent impedance of the AR. For simplicity, the primary and secondary resonant frequencies are set to be equal to ω_0 that satisfies

$$\omega_0 = \frac{1}{\sqrt{L_1 C_1}} = \frac{1}{\sqrt{L_2 C_2}}. \tag{1}$$

B. Basic Theory Analysis

As a kind of power supply, the WPTS should first obtain the required output voltage. Moreover, to enhance the system transfer efficiency and reduce EMI, ZVS of all switches in the WPTS should also be achieved. In this article, a JC-VZA is proposed by adjusting three control variables. The inverter is controlled by adjusting the duty cycle D_p and the AR is controlled by adjusting the duty cycle D_s and power angle δ.

The operating waveforms of the inverter and the AR are shown in Fig. 2. In Fig. 2(a), the phase shift angle of the inverter can be represented as φ_p ($\varphi_p = D_p\pi$, $0 < D_p < 1$). v_{ab1} is the fundamental waveform of the output ac square voltage of the inverter v_{ab}. Therefore, the rms value of v_{ab1}, U_1, can be calculated by

$$U_1[D_p] = \frac{2\sqrt{2}}{\pi} V_1 \sin\left[\frac{D_p\pi}{2}\right]. \tag{2}$$
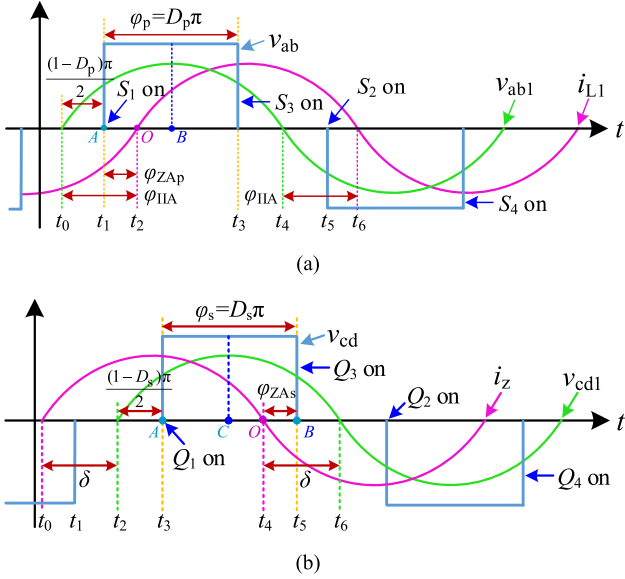
(a)

(b)

Fig. 2. Operating waveforms of the WPTS with JC-VZA (a) in the primary inverter and (b) in the secondary AR.

In Fig. 2(b), the phase shift angle of the AR can be represented as φ_s ($\varphi_s = D_s\pi$, $0 < D_s < 1$). v_{cd1} is the fundamental waveform of the input ac square voltage of the AR, v_{cd}. Similarly, the rms value of v_{cd1}, U_2, can be calculated by

$$U_2[D_s] = \frac{2\sqrt{2}}{\pi} V_2 \sin \left[\frac{D_s\pi}{2} \right]. \tag{3}$$

i_z ($-i_{L2}$) is the secondary inductor current and its rms value is represented as I_z (I_{L2}). Therefore, the power angle δ is defined as the phase difference between i_z and v_{cd1}. According to the basic circuit theory, the input active power of the AR, P_{irec}, can be obtained by

$$P_{irec}[D_s, \delta] = U_2 I_z \cos[-\delta] = \frac{2\sqrt{2}}{\pi} V_2 I_z \sin \left[\frac{D_s\pi}{2} \right] \cos[\delta]. \tag{4}$$

According to (4), if the direction of power flow is from V_1 to V_2, δ should be limited as $-\pi/2 < \delta < \pi/2$. Based on the active power conservation, if the power loss of the AR is ignored, it can be obtained that

$$P_{irec}[D_s, \delta] = V_2 I_2. \tag{5}$$

Based on (4) and (5), I_z can be obtained by

$$I_z[D_s, \delta] = I_2 \frac{\pi}{2\sqrt{2}} \csc \left[\frac{D_s\pi}{2} \right] \sec[\delta]. \tag{6}$$

C. Transfer Power Surface

Based on Fig. 1(b), when (1) is satisfied with R_1 and R_2 neglected, the voltage vectors satisfy

$$\begin{cases} \dot{U}_1 = j\omega_0 M \dot{I}_{L2} = -j\omega_0 M \dot{I}_z \\ \dot{U}_2 = j\omega_0 M \dot{I}_{L1}. \end{cases} \tag{7}$$
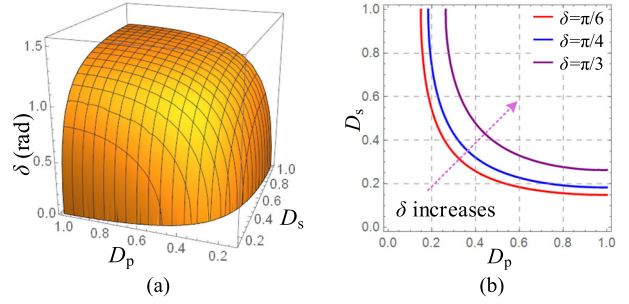

(a)   (b)

Fig. 3. Relationship between D_p, D_s, and δ when $P_u = 0.2$. (a) δ versus D_p and D_s. (b) D_s versus D_p with different δ.

Substituting (2) and (6) into (7), the output current I_2 can be obtained by

$$I_2[D_p, D_s, \delta] = \frac{8V_1}{\pi^2 \omega_0 M} \sin \left[\frac{D_p\pi}{2} \right] \sin \left[\frac{D_s\pi}{2} \right] \cos[\delta]. \tag{8}$$

Based on (8), the transfer power P_2 can be obtained by

$$P_2[D_p, D_s, \delta] = \frac{8V_1 V_2}{\pi^2 \omega_0 M} \sin \left[\frac{D_p\pi}{2} \right] \sin \left[\frac{D_s\pi}{2} \right] \cos[\delta]. \tag{9}$$

According to (9), when $D_p = D_s = 1$ and $\delta = 0$, the maximum transfer power P_{2max} is

$$P_{2max} = \frac{8V_1 V_2}{\pi^2 \omega_0 M}. \tag{10}$$

According to the maximum transfer power P_{2max}, the per-unit value of the transfer power, P_u, can be defined as

$$P_u = \frac{P_2}{P_{2max}} = \sin \left[\frac{D_p\pi}{2} \right] \sin \left[\frac{D_s\pi}{2} \right] \cos[\delta]. \tag{11}$$

In fact, (11) is the transfer power model with three control variables D_p, D_s, and δ. When P_u is fixed as 0.2, (11) including these three control variables makes up a transfer power surface, which is shown in Fig. 3(a). With different δ and a fixed P_u, the relationship between D_p and D_s is plotted in Fig. 3(b). As δ gradually increases, the control variables D_p and D_s gradually increase, and the combinations between D_p and D_s gradually shrink. Next, the ZVS region should be identified in the transfer power surface to reduce switching losses of the WPTS.

III. ZVS CONDITIONS WITH JC-VZA

Generally speaking, ZVS operation of MOSFET switches is significant to the inverter and the AR in the WPTS to reduce switching losses and EMI [20]–[24]. In this section, ZVS conditions and ZVS region in the transfer power surface are investigated in detail.

A. Conditions for Achieving ZVS

ZVS operation in the WPTS can be divided into two parts: ZVS of the AR and ZVS of the inverter.

1) ZVS of AR: As shown in Fig. 2(b), the moments when the switches $Q_1 \sim Q_4$ of the AR turn ON are labeled. Since the phase shift control is applied, the driver pulses of Q_1 and

Q_2 are complementary, and so do the driver pulses of Q_3 and Q_4. If Q_1 and Q_3 can achieve ZVS, Q_2 and Q_4 must achieve ZVS. Therefore, we only need to focus on ZVS realization of Q_1 and Q_3. In practice, ZVS is obtained by ensuring that MOSFET switches turn ON with drain-source voltage clamped to zero by conducting the antiparallel diode. Therefore, when a MOSFET switch turns ON, its antiparallel diode must be conducted in advance. Based on Figs. 1(a) and 2(b), the conditions for achieving ZVS in the AR can be summarized as

$$i_{\mathrm{z}}(t_3) \geq 0 \quad \text{and} \quad i_{\mathrm{z}}(t_5) \leq 0. \tag{12}$$

In Fig. 2(b), the phase difference between the point O and point B can be defined as φ_{ZAs}. Therefore, the conditions for realizing ZVS in the AR can be equivalent to

$$\varphi_{\mathrm{ZAs}} \geq 0°. \tag{13}$$

Based on Fig. 2(b), φ_{ZAs} can be represented as

$$\varphi_{\mathrm{ZAs}} = \delta - (1 - D_{\mathrm{s}})\pi/2. \tag{14}$$

To ensure $\varphi_{\mathrm{ZAs}} \geq 0°$, δ must be much larger than $0°$. In addition, in consideration of the power flow from V_1 to V_2, δ must be in the range from $-\pi/2$ to $\pi/2$. In a word, δ must satisfy

$$(1 - D_{\mathrm{s}})\pi/2 \leq \delta \leq \pi/2. \tag{15}$$

2) ZVS of Inverter: The process to analyze ZVS of the inverter is similar to the AR. The operating waveforms of the inverter are shown in Fig. 2(a). The conditions for achieving ZVS in the inverter can be obtained as

$$i_{\mathrm{L1}}(t_1) \leq 0 \quad \text{and} \quad i_{\mathrm{L1}}(t_3) \geq 0. \tag{16}$$

Likewise, the conditions for realizing ZVS in the inverter can be equivalent to

$$\varphi_{\mathrm{ZAp}} \geq 0°. \tag{17}$$

In Fig. 2(a), φ_{ZAp} can be represented as

$$\varphi_{\mathrm{ZAp}} = \varphi_{\mathrm{IIA}} - (1 - D_{\mathrm{p}})\pi/2. \tag{18}$$

Based on [20, Eq. (7)] and (1), when R_1 and R_2 are neglected, the input impedance of the resonant network is given as

$$Z_{\mathrm{in}} = \omega_0^2 M^2/(|Z_{\mathrm{E}}| \angle - \delta) = (\omega_0^2 M^2/|Z_{\mathrm{E}}|)\angle\delta. \tag{19}$$

Based on (19), the input impedance angle of the resonant network is equal to the power angle δ. Therefore, φ_{ZAp} can also be represented as

$$\varphi_{\mathrm{ZAp}} = \delta - (1 - D_{\mathrm{p}})\pi/2. \tag{20}$$

Likewise, to ensure $\varphi_{\mathrm{ZAp}} \geq 0°$, δ must be much larger than $0°$. In addition, in consideration of the power flow from V_1 to V_2, δ must satisfy

$$(1 - D_{\mathrm{p}})\pi/2 \leq \delta \leq \pi/2. \tag{21}$$

Based on (15) and (21), the critical conditions to achieve ZVS for the inverter and the AR can be obtained when $\varphi_{\mathrm{ZAp}} = 0°$ and $\varphi_{\mathrm{ZAs}} = 0°$, respectively, which are

$$\begin{aligned} \delta &= (1 - D_{\mathrm{p}})\pi/2 \cdots (\mathrm{B1}) - \text{for inverter} \\ \delta &= (1 - D_{\mathrm{s}})\pi/2 \cdots (\mathrm{B2}) - \text{for AR}. \end{aligned} \tag{22}$$
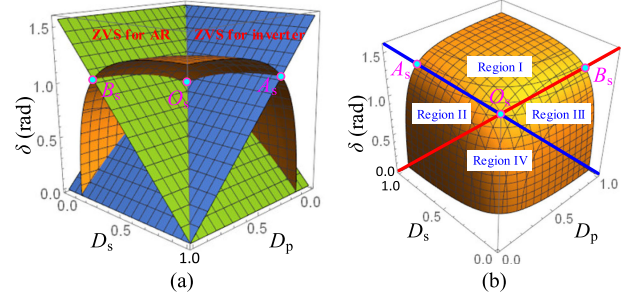

Fig. 4. Transfer power surface with ZVS conditions when $P_{\mathrm{u}} = 0.2$. (a) From the front. (b) From the back.

TABLE I
ZVS STATES OF INVERTER AND AR

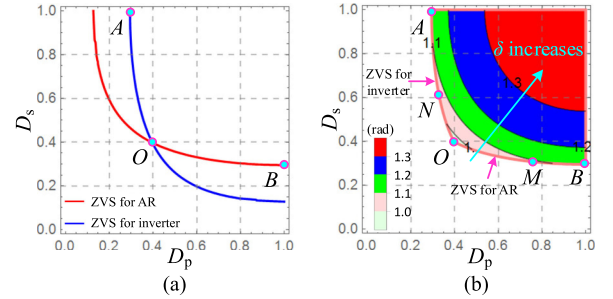|	Region I	Region II	Region III	Region IV
Inverter	ZVS	No ZVS	ZVS	No ZVS
Rectifier	ZVS	ZVS	No ZVS	No ZVS

Fig. 5. ZVS conditions for the inverter and the AR when $P_{\mathrm{u}} = 0.2$. (a) Projections of intersection lines between ZVS conditions and the transfer power surface. (b) Contour plot of δ in Region I.

B. ZVS Region in Transfer Power Surface

In consideration of critical ZVS conditions for the inverter and the AR in (22), the transfer power surface is replotted in Fig. 4. As shown in Fig. 4, the surface can be divided into four parts by ZVS conditions. Then, the inverter and the AR will operate in different ZVS states in these regions that are listed in Table I. Obviously, only in Region I, the WPTS can achieve ZVS of all switches. According to (11), if the required transfer power is assigned, δ can be obtained by

$$\delta = \arccos\left[\frac{P_{\mathrm{u}}}{\sin[D_{\mathrm{p}}\pi/2]\sin[D_{\mathrm{s}}\pi/2]}\right]. \tag{23}$$

Substituting (23) into (22), two space curves can be obtained. In practice, these two space curves are the intersection lines between two ZVS planes and the transfer power surface, respectively, in Fig. 4(a). The projections of these two space curves on the D_{p}–D_{s} plane are plotted in Fig. 5(a). If the WPTS runs along the blue line, the inverter can achieve ZVS critically. Likewise, if the WPTS runs along the red line, the AR can achieve ZVS critically. According to the previous analysis, if the control variables are above the two solid lines, the WPTS can achieve ZVS of all switches. By considering the transfer power
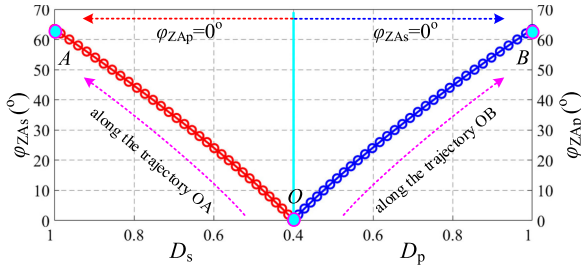
Fig. 6.   Relationship between φ_{ZAp} (φ_{ZAs}) and D_{p} (D_{s}) on the boundary curves when $P_{\mathrm{u}} = 0.2$.

and two ZVS conditions synthetically, the practical operating ranges of D_{p} and D_{s} will be limited to the closed region with solid pink lines in Fig. 5(b). Compared with the inner region, the boundary curves OA and OB tend to reduce the power loss of the WPTS in a fixed transfer power, which will be analyzed in Section IV. Here, some features on boundary curves should be analyzed in advance.

C. ZVS Angles on Boundary Curves

As shown in Fig. 5, when the operating point of the WPTS is on the trajectory OA, $\varphi_{\mathrm{ZAp}} = 0°$ and φ_{ZAs} changes along the trajectory OA. Substituting (22).(B1) into (14), it can be acquired that

$$\varphi_{\mathrm{ZAs}} = \delta - (1 - D_{\mathrm{s}})\pi/2 = (D_{\mathrm{s}} - D_{\mathrm{p}})\pi/2. \quad (24)$$

As shown in Fig. 5(b), on the trajectory OA, D_{p} is the monotonic decreasing function of D_{s}. Based on (24), φ_{ZAs} is the monotonic increasing function of D_{s}. When $\varphi_{\mathrm{ZAp}} = 0°$, the relationship between φ_{ZAs} and D_{s} is plotted in Fig. 6. When the operating point moves from the point O to the point A, φ_{ZAs} gradually increases from 0° while $\varphi_{\mathrm{ZAp}} = 0°$. Similarly, if the operating point is set on the trajectory OB, $\varphi_{\mathrm{ZAs}} = 0°$ and φ_{ZAp} will gradually change along the trajectory OB. Substituting (22).(B2) into (20), it can be obtained that

$$\varphi_{\mathrm{ZAp}} = \delta - (1 - D_{\mathrm{p}})\pi/2 = (D_{\mathrm{p}} - D_{\mathrm{s}})\pi/2. \quad (25)$$

Obviously, φ_{ZAp} on the trajectory OB has the similar characteristics with φ_{ZAs} on the trajectory OA. When $\varphi_{\mathrm{ZAs}} = 0°$, the relationship between φ_{ZAp} and D_{p} is also plotted in Fig. 6. As can be seen, φ_{ZAp} is the monotonic increasing function of D_{p}. In other words, when the operating point moves from the point O to the point B, φ_{ZAp} gradually increases while $\varphi_{\mathrm{ZAs}} = 0°$. Generally speaking, by setting different φ_{ZAp} when $\varphi_{\mathrm{ZAs}} = 0°$ or different φ_{ZAs} when $\varphi_{\mathrm{ZAp}} = 0°$, respectively, the operating point of the WPTS can be moved along the boundary curves freely.

IV. POWER LOSS ANALYSIS AND OPTIMAL ZVS ANGLES

According to the previous analysis, when the WPTS operates in Region I, all switches of the WPTS can achieve ZVS. Therefore, the key point is to find out an appropriate operating point to minimize the power loss.

A. Analysis of Power Loss in WPTS

The power losses of the WPTS can be divided into three parts: the power loss of the inverter P_{inv}, the power loss of the resonant network P_{res}, and the power loss of the AR P_{rec}.

1) Power Loss in Resonant Network: In practical applications, the power loss of the resonant network roughly include the conduction loss of coils, the radiation loss of coils, and the conduction loss of capacitors. The radiation loss of coils can be ignored due to the lower resonant frequency ($<$100 kHz) [15]. For simplicity, we use the constant ESRs (R_1 and R_2) to evaluate the power loss of the resonant network, P_{res}, which can be obtained by

$$P_{\mathrm{res}} = I_{\mathrm{L1}}^2 R_1 + I_{\mathrm{L2}}^2 R_2. \quad (26)$$

According to (2), (3), and (7), I_{L1} and I_{L2} can be obtained by

$$\begin{cases} I_{\mathrm{L1}} = \dfrac{U_2}{\omega_0 M} = \dfrac{2\sqrt{2}V_2}{\pi \omega_0 M} \sin\left[\dfrac{D_{\mathrm{s}}\pi}{2}\right] \\ I_{\mathrm{L2}} = \dfrac{U_1}{\omega_0 M} = \dfrac{2\sqrt{2}V_1}{\pi \omega_0 M} \sin\left[\dfrac{D_{\mathrm{p}}\pi}{2}\right]. \end{cases} \quad (27)$$

2) Power Losses in Inverter and AR: The power losses in the inverter and the AR share similar characteristics. Commonly, P_{inv} and P_{rec} can be represented as

$$\begin{cases} P_{\mathrm{inv}} = P_{\mathrm{inv\_sw}} + P_{\mathrm{inv\_con}} \\ P_{\mathrm{rec}} = P_{\mathrm{rec\_sw}} + P_{\mathrm{rec\_con}} \end{cases} \quad (28)$$

where $P_{\mathrm{inv\_sw}}$ and $P_{\mathrm{inv\_con}}$ are the switching and conduction losses of the inverter, respectively. Similarly, $P_{\mathrm{rec\_sw}}$ and $P_{\mathrm{rec\_con}}$ are the switching and conduction losses of the AR, respectively. If the inverter and the AR operate in Region I, their switching losses can be ignored approximately. Then, only the conduction losses should be considered. When the turn-on resistance of a power switch is represented as R_{dson}, the total power loss of the WPTS can be reckoned as P'_{res}, which can be obtained by

$$\begin{aligned} P'_{\mathrm{res}} &\approx P_{\mathrm{inv\_con}} + P_{\mathrm{res}} + P_{\mathrm{rec\_con}} \\ &= 2I_{\mathrm{L1}}^2 R_{\mathrm{dson}} + (I_{\mathrm{L1}}^2 R_1 + I_{\mathrm{L2}}^2 R_2) + 2I_{\mathrm{L2}}^2 R_{\mathrm{dson}} \\ &= I_{\mathrm{L1}}^2 (R_1 + 2R_{\mathrm{dson}}) + I_{\mathrm{L2}}^2 (R_2 + 2R_{\mathrm{dson}}) \\ &= I_{\mathrm{L1}}^2 R'_1 + I_{\mathrm{L2}}^2 R'_2 \end{aligned} \quad (29)$$

where R'_1 and R'_2 can be represented as

$$\begin{cases} R'_1 = R_1 + 2R_{\mathrm{dson}} \\ R'_2 = R_2 + 2R_{\mathrm{dson}}. \end{cases} \quad (30)$$

B. Derivation of Minimum Power Loss

To identify the optimal operating point with the minimum power loss, P'_{res} in Region I will be analyzed in detail. This process to find out the optimal operating point can be divided into two steps. The first step is to find out the minimum power loss region (MPLR). The second step is to find out the minimum power loss point in MPLR.

1) MPLR: Substituting (27) into (29), P'_{res} can be obtained as

$$P'_{\text{res}} = \frac{8}{\pi^2 \omega_0^2 M^2} \left(R'_2 V_1^2 \sin^2 \left[\frac{D_{\text{p}} \pi}{2} \right] + R'_1 V_2^2 \sin^2 \left[\frac{D_{\text{s}} \pi}{2} \right] \right). \tag{31}$$

In Region I, the constraint conditions can be summed up to two parts. One part is the transfer power model in (11) and the other is ZVS conditions for both sides of the WPTS in (15) and (21). They are summarized as

$$A : P_{\text{u}} = \sin \left[\frac{D_{\text{p}} \pi}{2} \right] \sin \left[\frac{D_{\text{s}} \pi}{2} \right] \cos [\delta]$$

$$B : \begin{cases} (1 - D_{\text{p}})\pi/2 \leq \delta \leq \pi/2 \cdots \text{(B1)} \\ (1 - D_{\text{s}})\pi/2 \leq \delta \leq \pi/2 \cdots \text{(B2)}. \end{cases} \tag{32}$$

Next, the power loss will be analyzed to identify MPLR. According to (32).B, ZVS conditions can be converted to

$$\begin{cases} 0 \leq \cos[\delta] \leq \cos[(1 - D_{\text{p}})\pi/2] = \sin[D_{\text{p}}\pi/2] \cdots \text{(B1)} \\ 0 \leq \cos[\delta] \leq \cos[(1 - D_{\text{s}})\pi/2] = \sin[D_{\text{s}}\pi/2] \cdots \text{(B2)}. \end{cases} \tag{33}$$

According to (32).A, it can be obtained that

$$\cos[\delta] = \frac{P_{\text{u}}}{\sin[D_{\text{p}}\pi/2] \sin[D_{\text{s}}\pi/2]}. \tag{34}$$

Substituting (34) into (33), it can be obtained that

$$\begin{cases} 0 \leq \dfrac{P_{\text{u}}}{\sin[D_{\text{s}}\pi/2]} \leq \sin^2 \left[\dfrac{D_{\text{p}} \pi}{2} \right] \cdots \text{(B1)} \\ 0 \leq \dfrac{P_{\text{u}}}{\sin[D_{\text{p}}\pi/2]} \leq \sin^2 \left[\dfrac{D_{\text{s}} \pi}{2} \right] \cdots \text{(B2)}. \end{cases} \tag{35}$$

According to (35).(B1) (ZVS for the inverter), the objective function (31) can be simplified as

$$P'_{\text{res}} \geq \frac{8}{\pi^2 \omega_0^2 M^2} \left(\frac{R'_2 V_1^2 P_{\text{u}}}{\sin[D_{\text{s}}\pi/2]} + R'_1 V_2^2 \sin^2 \left[\frac{D_{\text{s}} \pi}{2} \right] \right). \tag{36}$$

The right-hand side of (36) is the power loss of the WPTS on the blue boundary curve shown in Fig. 5(a). The physical meaning of (36) is that the minimum power loss must be achieved on the blue boundary curve when the inverter achieves ZVS. Similarly, according to (35).(B2) (ZVS for the AR), the objective

function (31) can be simplified as

$$P'_{\text{res}} \geq \frac{8}{\pi^2 \omega_0^2 M^2} \left(R'_2 V_1^2 \sin^2 \left[\frac{D_{\text{p}} \pi}{2} \right] + \frac{R'_1 V_2^2 P_{\text{u}}}{\sin[D_{\text{p}}\pi/2]} \right). \tag{37}$$

Likewise, according to (37), the minimum power loss must be obtained on the red boundary curve shown in Fig. 5(a) when the AR achieves ZVS. In consideration of ZVS conditions for both sides, the minimum value must be located at the combination boundary (the trajectory AOB) shown in Fig. 5(b). Therefore, MPLR must be a part of the trajectory AOB.

2) Minimum Power Loss Point: Next step is to find the minimum power loss point in MPLR. According to (36), the power loss can be rearranged as (38), shown at the bottom of this page, where the condition for achieving the minimum value is

$$R'_2 V_1^2 \frac{P_{\text{u}}}{2 \sin[D_{\text{s}}\pi/2]} = R'_1 V_2^2 \sin^2 \left[\frac{D_{\text{s}} \pi}{2} \right]. \tag{39}$$

According to (39), D_{s} can be obtained by

$$D_{\text{s}} = \frac{2}{\pi} \arcsin \left[\frac{R'_2 V_1^2 P_{\text{u}}}{2 R'_1 V_2^2} \right]^{\frac{1}{3}} = \frac{2}{\pi} \arcsin \left[\frac{R'_2 P_{\text{u}}}{2 R'_1 K_{\text{cv}}^2} \right]^{\frac{1}{3}} = D_{\text{s}1} \tag{40}$$

where K_{cv} is the voltage gain of the WPTS, which is defined as V_2/V_1. Substituting (22). (B1) and (40) into (32).A, D_{p} on the boundary curve for achieving ZVS in the inverter can be obtained as

$$D_{\text{p}} = \frac{2}{\pi} \arcsin \left[\sqrt{2} P_{\text{u}} K_{\text{cv}} \sqrt{\frac{R'_1}{R'_2}} \right]^{\frac{1}{3}} = D_{\text{p}1}. \tag{41}$$

Similarly, according to (37), the power loss can be rearranged as (42), shown at the bottom of this page, where the condition for achieving the minimum value is

$$R'_2 V_1^2 \sin^2 \left[\frac{D_{\text{p}} \pi}{2} \right] = R'_1 V_2^2 \frac{P_{\text{u}}}{2 \sin[D_{\text{p}}\pi/2]}. \tag{43}$$

According to (43), D_{p} can be obtained by

$$D_{\text{p}} = \frac{2}{\pi} \arcsin \left[\frac{R'_1 P_{\text{u}} K_{\text{cv}}^2}{2 R'_2} \right]^{\frac{1}{3}} = D_{\text{p}2}. \tag{44}$$

$$P'_{\text{res}} \geq \frac{8}{\pi^2 \omega_0^2 M^2} \left(R'_2 V_1^2 \frac{P_{\text{u}}}{2 \sin[D_{\text{s}}\pi/2]} + R'_2 V_1^2 \frac{P_{\text{u}}}{2 \sin[D_{\text{s}}\pi/2]} + R'_1 V_2^2 \sin^2 \left[\frac{D_{\text{s}} \pi}{2} \right] \right) \geq \frac{24}{\pi^2 \omega_0^2 M^2} \left[\frac{V_1^4 V_2^2 R'_1 {R'_2}^2 P_{\text{u}}^2}{4} \right]^{\frac{1}{3}} \tag{38}$$

$$P'_{\text{res}} \geq \frac{8}{\pi^2 \omega_0^2 M^2} \left(R'_1 V_2^2 \frac{P_{\text{u}}}{2 \sin[D_{\text{p}}\pi/2]} + R'_1 V_2^2 \frac{P_{\text{u}}}{2 \sin[D_{\text{p}}\pi/2]} + R'_2 V_1^2 \sin^2 \left[\frac{D_{\text{p}} \pi}{2} \right] \right) \geq \frac{24}{\pi^2 \omega_0^2 M^2} \left[\frac{V_1^2 V_2^4 {R'_1}^2 R'_2 P_{\text{u}}^2}{4} \right]^{\frac{1}{3}} \tag{42}$$

TABLE II
OPERATING CONDITIONS AND THE MINIMUM POWER LOSS

Case	Region	Operating Points (D_p, D_s)	Conditions	Power Loss
I	Point A	$\begin{cases} D_p = \dfrac{2}{\pi}\arcsin(P_u)^{\frac{1}{2}} \\ D_s = 1 \end{cases}$	$P_u \geq \dfrac{2R_1' K_{cv}^2}{R_2'} = P_{uc1}$ and $K_{cv} < \sqrt{\dfrac{R_2'}{2R_1'}}$	$\dfrac{8}{\pi^2 \omega_0^2 M^2}(R_2' V_1^2 P_u + R_1' V_2^2)$
II	Trajectory AO	$\begin{cases} D_p = \dfrac{2}{\pi}\arcsin\left(\sqrt{2}P_u K_{cv}\sqrt{\dfrac{R_1'}{R_2'}}\right)^{\frac{1}{3}} \\ D_s = \dfrac{2}{\pi}\arcsin\left(\dfrac{R_2' P_u}{2R_1' K_{cv}^2}\right)^{\frac{1}{3}} \end{cases}$	$P_u < \dfrac{2R_1' K_{cv}^2}{R_2'} = P_{uc1}$ and $K_{cv} < \sqrt{\dfrac{R_2'}{2R_1'}}$	$\dfrac{24}{\pi^2 \omega_0^2 M^2}\left[\dfrac{V_1^4 V_2^2 R_1' R_2'^2 P_u^2}{4}\right]^{\frac{1}{3}}$
III	Point O	$D_p = D_s = \dfrac{2}{\pi}\arcsin\left(P_u\right)^{\frac{1}{3}}$	$\sqrt{\dfrac{R_2'}{2R_1'}} \leq K_{cv} \leq \sqrt{\dfrac{2R_2'}{R_1'}}$	$\dfrac{8P_u^{2/3}}{\pi^2 \omega_0^2 M^2}(R_2' V_1^2 + R_1' V_2^2)$
IV	Trajectory OB	$\begin{cases} D_p = \dfrac{2}{\pi}\arcsin\left(\dfrac{R_1' P_u K_{cv}^2}{2R_2'}\right)^{\frac{1}{3}} \\ D_s = \dfrac{2}{\pi}\arcsin\left(\dfrac{\sqrt{2}P_u}{K_{cv}}\sqrt{\dfrac{R_2'}{R_1'}}\right)^{\frac{1}{3}} \end{cases}$	$P_u < \dfrac{2R_2'}{R_1' K_{cv}^2} = P_{uc2}$ and $K_{cv} > \sqrt{\dfrac{2R_2'}{R_1'}}$	$\dfrac{24}{\pi^2 \omega_0^2 M^2}\left[\dfrac{V_1^2 V_2^4 R_1'^2 R_2' P_u^2}{4}\right]^{\frac{1}{3}}$
V	Point B	$\begin{cases} D_p = 1 \\ D_s = \dfrac{2}{\pi}\arcsin(P_u)^{\frac{1}{2}} \end{cases}$	$P_u \geq \dfrac{2R_2'}{R_1' K_{cv}^2} = P_{uc2}$ and $K_{cv} > \sqrt{\dfrac{2R_2'}{R_1'}}$	$\dfrac{8}{\pi^2 \omega_0^2 M^2}(R_2' V_1^2 + R_1' V_2^2 P_u)$

Substituting (22).(B2) and (44) into (32).A, D_s on boundary conditions for achieving ZVS in the AR can be obtained as

$$D_s = \frac{2}{\pi}\arcsin\left[\frac{\sqrt{2}P_u}{K_{cv}}\sqrt{\frac{R_2'}{R_1'}}\right]^{\frac{1}{3}} = D_{s2}. \qquad (45)$$

According to Fig. 5(b), the operating point $N(D_{p1}, D_{s1})$ should be located at the boundary trajectory OA and $M(D_{p2}, D_{s2})$ should be located at the boundary trajectory OB. Otherwise, the inverter and the AR cannot achieve ZVS simultaneously. Substituting (22).(B1) and (B2) into (32).A at the same time, the operating point O can be obtained by

$$D_{po} = D_{so} = \frac{2}{\pi}\arcsin\left[P_u\right]^{\frac{1}{3}}. \qquad (46)$$

On the one hand, if the operating point $N(D_{p1}, D_{s1})$ is limited on the boundary trajectory OA, the control variable D_{s1} should satisfy

$$\begin{cases} D_{s1} > D_{so} \cdots (a) \\ 1 > D_{s1} \cdots (b). \end{cases} \qquad (47)$$

Based on (40) and (47).(a), we can obtain

$$K_{cv} < \sqrt{R_2'/2R_1'}. \qquad (48)$$

In addition, according to (40) and (47).(b), we can obtain

$$P_u < \frac{2R_1' K_{cv}^2}{R_2'} = P_{uc1}. \qquad (49)$$

If (48) can be satisfied, the minimum power loss point can be limited to the upper side of the point O in blue line of Fig. 5(a). Otherwise, the minimum power loss point should be set at the point O to ensure ZVS of the AR. Moreover, if (49) can be satisfied at the same time, it means the minimum power loss

point will be located on the boundary trajectory OA (except point O and point A). Otherwise, the minimum power loss point will be set at point A.

On the other hand, if the operating point $M(D_{p2}, D_{s2})$ is limited on the boundary trajectory OB, the control variable D_{p2} should satisfy

$$\begin{cases} D_{p2} > D_{po} \cdots (a) \\ 1 > D_{p2} \cdots (b). \end{cases} \qquad (50)$$

Based on (44) and (50).(a), it can be obtained that

$$K_{cv} > \sqrt{2R_2'/R_1'}. \qquad (51)$$

Moreover, based on (44) and (50).(b), it can be obtained that

$$P_u < \frac{2R_2'}{R_1' K_{cv}^2} = P_{uc2}. \qquad (52)$$

If (51) can be satisfied, the minimum power loss point can be limited into the lower side of point O in the red line of Fig. 5(a). Otherwise, the minimum power loss point should be set at the point O to ensure ZVS of the inverter. Moreover, if (52) can be satisfied at the same time, it means the minimum power loss point will be limited on the boundary trajectory OB (except point O and point B). Otherwise, the minimum power loss point will be set at point B.

According to the previous analysis, if both (48) and (51) cannot be satisfied, the operating point to minimize the power loss should be set at point O to ensure ZVS of two sides. Their conditions are

$$\sqrt{R_2'/2R_1'} \leq K_{cv} \leq \sqrt{2R_2'/R_1'}. \qquad (53)$$

In consideration of all cases, the conclusions to obtain the minimum power loss are summarized in Table II. According to different K_{cv} and P_u, the operating cases to minimize the power

TABLE III
SYSTEM PARAMETERS USED IN CALCULATION

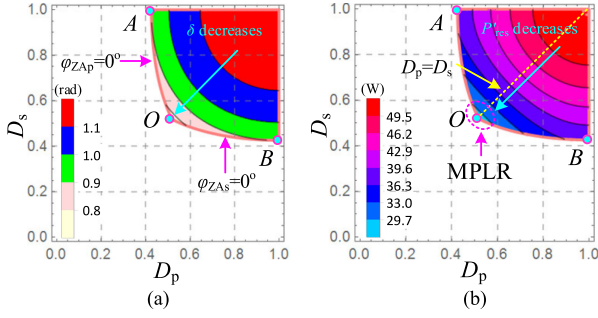| Symbol	Quantity	Value
L_1, L_2	resonant inductances	116.86μH
C_1, C_2	resonant capacitances	30nF
R_1, R_2	equivalent series resistances	0.2Ω
k	coupling coefficient	0.1
ω_0	resonant angular frequency	5.34×10^5rad/s
f_0	resonant frequency	85kHz
R_L	load resistance	10Ω

Fig. 7. Contour plots of δ and P'_{res} with D_p and D_s, when $V_1 = 80$ V, $V_2 = 80$ V, $I_2 = 4$ A, $R_L = 20$ Ω, $K_{cv} = 1$, and $P_u = 0.385$. (a) Contour plot of δ in Region I. (b) Contour plot of P'_{res} in Region I.

Fig. 8. Contour plots of P'_{res} with D_p and D_s. (a) Contour plot of P'_{res} in Region I, when $V_1 = 80$ V, $V_2 = 60$ V, $I_2 = 4$ A, $R_L = 15$ Ω, $K_{cv} = 0.75$, and $P_u = 0.385$. (b) Contour plot of P'_{res} in Region I, when $V_1 = 60$ V, $V_2 = 80$ V, $I_2 = 3$ A, $R_L = 26.7$ Ω, $K_{cv} = 1.33$, and $P_u = 0.385$.

Fig. 9. P'_{res} on the boundary curve AOB with different operating situations in Case III.

loss on the combination boundary curves can be classified into five kinds. The corresponding operating points, power losses, and operating conditions are also listed in Table II.

C. Theoretical Verification

As shown in Table II, when K_{cv} and P_u change, the minimum power loss point of the WPTS will change accordingly. Next, the conclusions in Table II will be proved by the theoretical calculation. For simplicity, it is assumed that $R'_1 = R'_2$ and the deadtime effect of the WPTS is ignored. The parameters for theoretical calculation are listed in Table III.

1) Case III: Case III will be validated first. When $V_1 = V_2 = 80$ V, $I_2 = 4$ A, $R_L = 20$ Ω, $K_{cv} = 1$, and $P_u = 0.385$, the contour plot of δ can be depicted in Fig. 7(a). According to the previous analysis in Section III-C, along the trajectory OA, φ_{ZAs} gradually increases when $\varphi_{ZAp} = 0°$. Similarly, along the trajectory OB, φ_{ZAp} gradually increases when $\varphi_{ZAs} = 0°$. Furthermore, the contour plot of P'_{res} is drawn in Fig. 7(b). P'_{res} is centered exactly on the line $D_p = D_s$. In addition, according to the distribution and variation tendency of the power loss in Region I, the WPTS will achieve the minimum power loss on the boundary AOB near point O that is located at the MPLR. Moreover, in Case III, the situation that V_1 is unequal to V_2 needs to be verified. When $1/\sqrt{2} \leq K_{cv} < 1$, the operating conditions for stepping down the output voltage are set as $V_1 = 80$ V, $V_2 = 60$ V, $I_2 = 4$ A, $R_L = 15$ Ω, $K_{cv} = 0.75$, and $P_u = 0.385$. When $1 < K_{cv} \leq \sqrt{2}$, the operating conditions for stepping up the output voltage are set as $V_1 = 60$ V, $V_2 = 80$ V, $I_2 = 3$ A, $R_L = 26.7$Ω, $K_{cv} = 1.33$, and $P_u = 0.385$. According to the parameters listed in Table III, the power loss distributions in Region I are plotted in Fig. 8. In Fig. 8(a), the MPLR inclines to
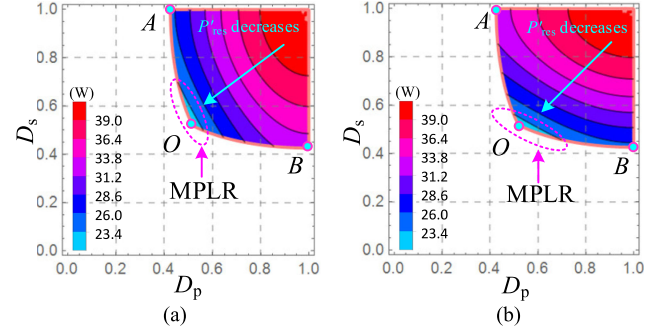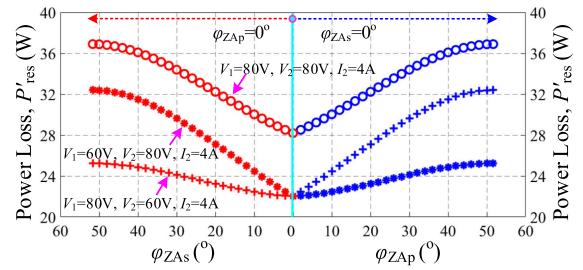
the boundary curve OA slightly. In Fig. 8(b), the MPLR inclines to the boundary curve OB slightly. However, according to the distribution and variation tendency of the power loss in Region I, the WPTS will achieve the minimum power loss on the boundary AOB near point O, which is also located at the MPLR.

To pinpoint the minimum power loss point, the power losses on the boundary AOB in these three situations are calculated and plotted in Fig. 9. In the left-hand side, P'_{res} is the monotonic increasing function of φ_{ZAs} when $\varphi_{ZAp} = 0°$. Similarly, in the right-hand side, P'_{res} is also the monotonic increasing function of φ_{ZAp} when $\varphi_{ZAs} = 0°$. Therefore, as long as K_{cv} is in the range from $1/\sqrt{2}$ to $\sqrt{2}$, the WPTS will always achieve the minimum power loss when $\varphi_{ZAp} = 0°$ and $\varphi_{ZAs} = 0°$ (at the point O). Then, the conclusions on Case III in Table II are well verified.

2) Case I and Case II: Next, Case I and II in Table II will be verified. In Table II, Case I satisfies $K_{cv} < 1/\sqrt{2}$ and $P_u \geq P_{uc1}$. Here, the operating conditions in Case I are set as $V_1 = 80$ V, $V_2 = 30$ V, $I_2 = 3$ A, $R_L = 10$ Ω, $K_{cv} = 0.375$, and $P_u = 0.289$. Likewise, Case II satisfies $K_{cv} < 1/\sqrt{2}$ and $P_u < P_{uc1}$. The operating conditions in Case II are set as $V_1 = 80$ V, $V_2 = 30$ V, $I_2 = 1.5$ A, $R_L = 20$ Ω, $K_{cv} = 0.375$, and $P_u = 0.144$. According to the parameters listed in Table III, the power loss distributions of these two situations are plotted in Fig. 10. In these two situations, the MPLRs incline to the boundary curve OA. According to the distribution and variation tendency of the power loss in Region I, the WPTS will achieve the minimum power loss on the boundary OA.

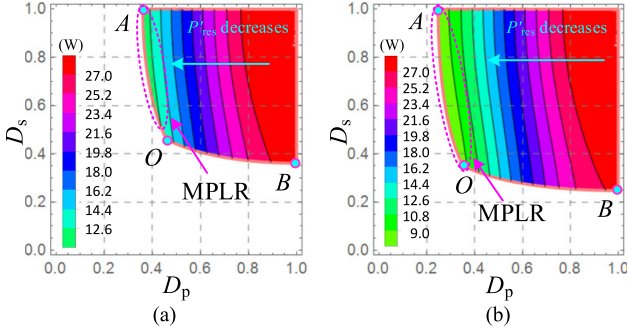Similarly, to find out the minimum power loss point, the power losses on the boundary AOB are calculated and plotted

Fig. 10. Contour plots of P'_{res} with D_{p} and D_{s}. (a) Contour plot of P'_{res} in Region I, when $V_1 = 80$ V, $V_2 = 30$ V, $I_2 = 3$ A, $R_{\text{L}} = 10$ Ω, $K_{\text{cv}} = 0.375$, and $P_{\text{u}} = 0.289$. (b) Contour plot of P'_{res} in Region I, when $V_1 = 80$ V, $V_2 = 30$ V, $I_2 = 1.5$ A, $R_{\text{L}} = 20$ Ω, $K_{\text{cv}} = 0.375$, and $P_{\text{u}} = 0.144$.
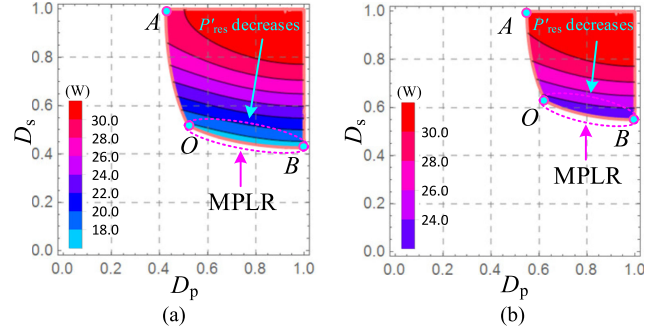
Fig. 12. Contour plots of P'_{res} with D_{p} and D_{s}. (a) Contour plot of P'_{res} in Region I, when $V_1 = 40$ V, $V_2 = 80$ V, $I_2 = 2$ A, $R_{\text{L}} = 40$ Ω, $K_{\text{cv}} = 2$, and $P_{\text{u}} = 0.385$. (b) Contour plot of P'_{res} in Region I, when $V_1 = 40$ V, $V_2 = 80$ V, $I_2 = 3$ A, $R_{\text{L}} = 26.7$ Ω, $K_{\text{cv}} = 2$, and $P_{\text{u}} = 0.577$.

Fig. 11. P'_{res} on the boundary curve AOB with different operating situations in Case I and Case II.
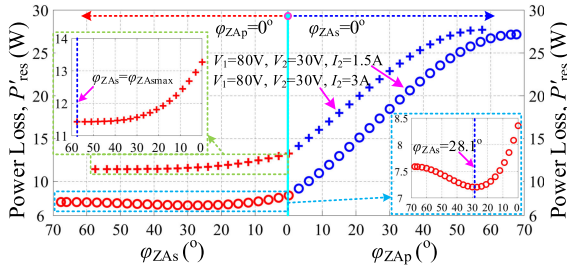

Fig. 13. P'_{res} on the boundary curve AOB with different operating situations in Cases IV and Case V.

in Fig. 11. When $V_1 = 80$ V, $V_2 = 30$ V, $I_2 = 3$ A, $R_{\text{L}} = 10$ Ω, $K_{\text{cv}} = 0.375$, and $P_{\text{u}} = 0.289$, P'_{res} is the monotonic decreasing function of φ_{ZAs} when $\varphi_{\text{ZAp}} = 0°$ in the left-hand side and the monotonic increasing function of φ_{ZAp} when $\varphi_{\text{ZAs}} = 0°$ in the right-hand side. Therefore, the WPTS will achieve the minimum power loss when $\varphi_{\text{ZAp}} = 0°$ and $\varphi_{\text{ZAs}} = \varphi_{\text{ZAmax}}$ (at the point A) theoretically. In this situation, since $K_{\text{cv}} < 1/\sqrt{2}$ and $P_{\text{u}} = 0.289 > 0.281 = P_{\text{uc1}}$, the correctness of conclusions on Case I is verified very well.

When $V_1 = 80$ V, $V_2 = 30$ V, $I_2 = 1.5$ A, $R_{\text{L}} = 20$ Ω, $K_{\text{cv}} = 0.375$, and $P_{\text{u}} = 0.144$, P'_{res} achieves the minimum power loss when $\varphi_{\text{ZAp}} = 0°$ and $\varphi_{\text{ZAs}} = 28.1°$ (a certain point on the trajectory OA). In this situation, since $K_{\text{cv}} < 1/\sqrt{2}$ and $P_{\text{u}} = 0.144 < 0.281 = P_{\text{uc1}}$, the correctness of conclusions on Case II is also verified very well.

3) Case IV and Case V: Finally, Cases IV and V in Table II will be verified. In Table II, Case IV satisfies $K_{\text{cv}} > \sqrt{2}$ and $P_{\text{u}} < P_{\text{uc2}}$. Here, the operating conditions in Case IV are set as $V_1 = 40$ V, $V_2 = 80$ V, $I_2 = 2$ A, $R_{\text{L}} = 40$ Ω, $K_{\text{cv}} = 2$, and $P_{\text{u}} = 0.385$. Likewise, Case V satisfies $K_{\text{cv}} > \sqrt{2}$ and $P_{\text{u}} \geq P_{\text{uc2}}$. The operating conditions in Case V are set as $V_1 = 40$ V, $V_2 = 80$ V, $I_2 = 3$ A, $R_{\text{L}} = 26.7$ Ω, $K_{\text{cv}} = 2$, and $P_{\text{u}} = 0.577$. According to the parameters listed in Table III, the power loss distributions of these two situations are plotted in Fig. 12. In these two situations, the MPLRs incline to the boundary curve OB. According to the distribution and variation tendency of the power loss in Region I, the WPTS will achieve the minimum power loss on the boundary OB.

Similarly, to find out the minimum power loss point, the power losses on the boundary AOB are calculated and plotted
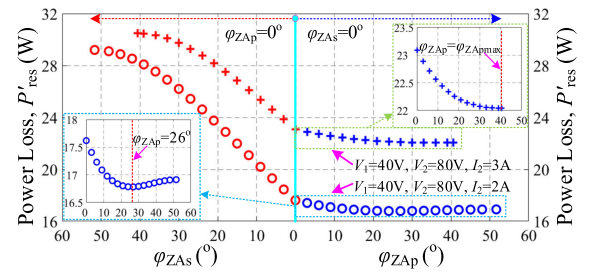
Fig. 13. When $V_1 = 40$ V, $V_2 = 80$ V, $I_2 = 3$ A, $R_{\text{L}} = 26.7$ Ω, $K_{\text{cv}} = 2$, and $P_{\text{u}} = 0.577$, P'_{res} is the monotonic increasing function of φ_{ZAs} when $\varphi_{\text{ZAp}} = 0°$ in the left-hand side and the monotonic decreasing function of φ_{ZAp} when $\varphi_{\text{ZAs}} = 0°$ in the right-hand side. Therefore, the WPTS will achieve the minimum power loss when $\varphi_{\text{ZAs}} = 0°$ and $\varphi_{\text{ZAp}} = \varphi_{\text{ZAmax}}$ (at the point B) theoretically. In this situation, since $K_{\text{cv}} > \sqrt{2}$ and $P_{\text{u}} = 0.577 > 0.5 = P_{\text{uc2}}$, the correctness of conclusions on Case V is verified very well. When $V_1 = 40$ V, $V_2 = 80$ V, $I_2 = 2$ A, $R_{\text{L}} = 40$ Ω, $K_{\text{cv}} = 2$, and $P_{\text{u}} = 0.385$, P'_{res} achieves the minimum power loss when $\varphi_{\text{ZAs}} = 0°$ and $\varphi_{\text{ZAp}} = 26°$ (a certain point on the trajectory OB). In this situation, since $K_{\text{cv}} > \sqrt{2}$ and $P_{\text{u}} = 0.385 < 0.5 = P_{\text{uc2}}$, the correctness of the conclusions on Case IV is also verified very well.

V. JC-VZA FOR DYNAMIC EFFICIENCY OPTIMIZATION

According to the previous analysis in Section IV, there is an optimal operating point to minimize the power loss on the boundary curves. Therefore, a vital step is to make the system operate at any point of boundary curves freely and stably to identify this operating point. A JC-VZA for dynamic efficiency optimization is proposed to achieve the required output and maximize the transfer efficiency of the WPTS by adjusting ZVS angles reasonably.

A. Joint Control With Variable ZVS Angles

The control block diagram of the proposed JC-VZA is shown in Fig. 14. This control strategy can be divided into two parts:
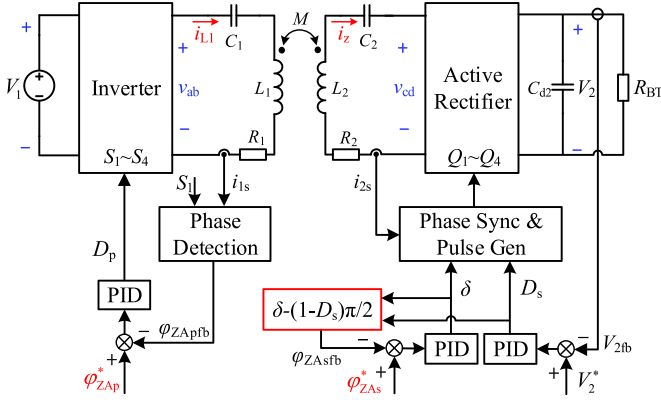
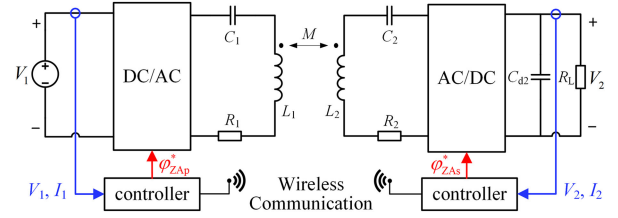Fig. 14. Control block diagram of the proposed JC-VZA.

Fig. 15. Control diagram of dynamic efficiency optimization method based on the proposed JC-VZA.

Fig. 16. Flowchart of the control logic to maximize the transfer efficiency.

the primary control, and the secondary control. On the one hand, the secondary control is comprised of two closed loops: the voltage loop and the ZVS angle loop of the AR. The basic ideas of the secondary control have two aspects. One aspect is to control the output voltage by changing D_s. The other is to control φ_{ZAs} by adjusting δ. On the other hand, the primary control is to regulate φ_{ZAp} by adjusting D_p. The operating principle and implementation of JC-VZA are briefly explained as follows.

1) Voltage Loop: In the secondary side, the controller samples V_2 directly and calculates the results through proportion-integration-differentiation (PID) algorithm according to V_2^* and V_{2fb}. Since the voltage closed loop is completely located at the secondary side without any communication, the reliability of the WPTS can be enhanced significantly.

2) ZVS Angle Loop of AR: To achieve the required ZVS angle of the AR, φ_{ZAs} must be controlled independently. However, D_s changes for controlling the required output voltage in real time, which leads to the change of φ_{ZAs} accordingly. Fortunately, according to (14), a simple decoupled control for the ZVS angle loop is proposed, which is marked in red box. Moreover, to decrease the effect of ZVS angle loop to the voltage loop, the setting time of ZVS angle loop is relatively longer than that of the voltage loop.

3) ZVS Angle Loop of Inverter: Likewise, in the primary side, φ_{ZAp} must be controlled independently to achieve the minimum power loss. The basic idea of the primary control is to change φ_{ZAp} by adjusting D_p. It is worth mentioning that the setting time of the ZVS angle loop in the primary side is relatively longer than that in the secondary side.

In addition, the phase-locked methods to acquire the resonant current in the primary and secondary sides have been published in [16] and [21] and will not be repeated. The proposed JC-VZA is implemented by two separated controllers in the primary and secondary sides without any synchronization, so it is easier and more feasible than the traditional TPS.

B. Efficiency Optimization Method

According to the previous conclusions in Table II, there are five cases and their optimal operating points are also listed. The control diagram of the efficiency optimization method is shown
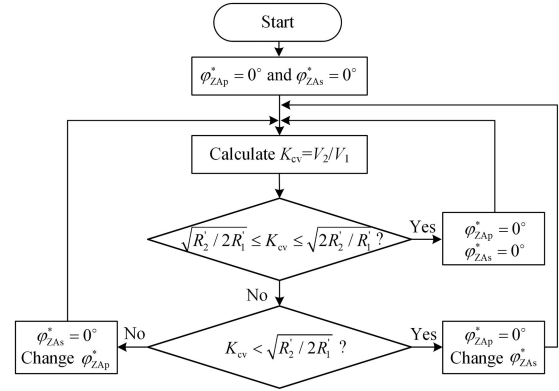
in Fig. 15. The primary and secondary controllers sample the dc currents and voltages of the inverter and the AR, respectively. Then, they exchange their sampling data with each other by wireless communication modules. According to V_1, I_1 and V_2, I_2, the controllers in the primary and secondary sides calculate K_{cv}, P_1, and P_2, respectively. Finally, they will decide how to change their own ZVS angles.

The detailed flowchart of control logic that each controller should follow is shown in Fig. 16. First, they need to calculate $K_{cv} = V_2/V_1$ and decide whether K_{cv} is in the range from $\sqrt{R_2'/2R_1'}$ to $\sqrt{2R_2'/R_1'}$. If it is true, both φ_{ZAp}^* and φ_{ZAs}^* should be set to $0°$ to make the WPTS operate at the point O to minimize the power loss. If K_{cv} is smaller than $\sqrt{R_2'/2R_1'}$, φ_{ZAp}^* needs to be set to $0°$ and φ_{ZAs}^* should be changed to make the operating point of the WPTS move along the trajectory OA and search for the minimum power loss point. If K_{cv} is larger than $\sqrt{2R_2'/R_1'}$, φ_{ZAs}^* needs to be set to $0°$ and φ_{ZAp}^* should be changed to make the operating point of the WPTS move along the trajectory OB and search for the minimum power loss point.

When the minimum power loss point is located on the OA or OB, P&O [15] is adopted to find out the minimum power loss point. To explain this process more clearly, take the search process on the trajectory OA as an example. Based on Table II and Fig. 16, the key point of the dynamic efficiency optimization method is to find out the optimal φ_{ZAs}^* to maximize the transfer efficiency in real time while $\varphi_{ZAp}^* = 0°$. The primary controller samples V_1, I_1, and sends them to the secondary controller through wireless communication modules. The secondary controller receives V_1, I_1 and samples V_2, I_2 by itself. Then, it will calculate the input power P_1, the output power P_2, and the overall transfer efficiency η_{sys} in real time. The secondary
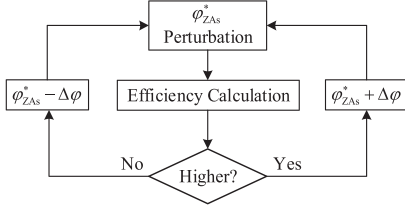
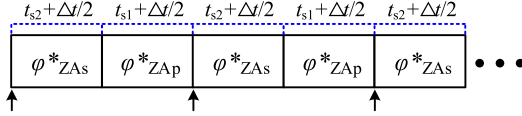Fig. 17.   Flowchart of the selection of the optimal ZVS angle in the AR.

Fig. 18.   Time intervals for dynamic efficiency optimization in the JC-VZA.

Fig. 19.   Experimental prototype.

controller perturbs φ_{ZAs}^* continuously and records the transfer efficiency of each step for the perturbation and reregulation. The direction of the perturbation is maintained for the next step if the efficiency gets higher; otherwise, it is reversed. Fig. 17 shows this flowchart.

C. Stability of JC-VZA for Dynamic Efficiency Optimization

When the dynamic efficiency optimization method is applied in the WPTS with JC-VZA, the system stability should be discussed.

1) Selection of Time Interval: To avoid the oscillations of the WPTS and improve the stability of the JC-VZA, it is significant to select an appropriate time interval for exchanging the information of two sides with wireless communication modules. The longest setting times of the step changes of ZVS angles in the primary and secondary sides are set as t_{s1} and t_{s2}, respectively. Therefore, the practical time interval for exchanging the information of two sides and changing the ZVS angles of two sides, T_{total}, should satisfy

$$T_{\mathrm{total}} = t_{\mathrm{s1}} + t_{\mathrm{s2}} + \Delta t \qquad (54)$$

where Δt should be larger than 0 to remain a time margin for dynamic regulation of the system. Since the communication time delay can be limited to hundreds of microseconds, it can be nearly ignored compared with Δt that commonly ranges from tens of milliseconds to hundreds of milliseconds. The time intervals for dynamic efficiency optimization in the JC-VZA are shown in Fig. 18. When the information exchange between two sides is finished, which is labeled with an arrow, the secondary-side controller updates φ_{ZAs}^* immediately and φ_{ZAs} begins to change accordingly while φ_{ZAp}^* is fixed and φ_{ZAp} maintains constant in the first time duration $t_{\mathrm{s2}} + \Delta t/2$. Subsequently, in the next time duration $t_{\mathrm{s1}} + \Delta t/2$, the primary-side controller updates φ_{ZAp}^* immediately and φ_{ZAp} begins to change accordingly while φ_{ZAs}^* is fixed and φ_{ZAs} maintains constant, until the next information exchange arrives. According to (54), the practical frequency f_{exc} for exchanging the information of two sides should satisfy

$$f_{\mathrm{exc}} = 1/T_{\mathrm{total}}. \qquad (55)$$
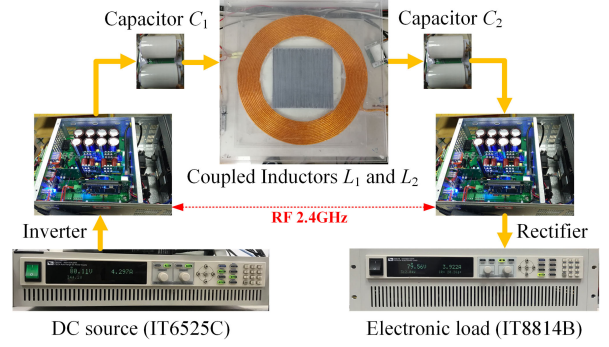
Obviously, it is important to shorten the setting time by adjusting the parameters of PID controllers in the JC-VZA to minimize t_{s1} and t_{s2} as much as possible, which is beneficial to quickly track the maximum transfer efficiency point of the WPTS.

2) Solution for Communication Interrupt: Although the communication interrupt occurs, the system reliability will be merely affected, because wireless communication modules are not used in the closed loop for voltage regulation. In other words, if the communication interrupt or error code happens accidentally, it is easy to deal with these problems by limiting the range of φ_{ZAp}^* or φ_{ZAs}^*. Although the maximum transfer efficiency cannot be achieved temporarily due to communication problems, the required output and safe operation of the WPTS can be guaranteed. Therefore, compared with the traditional control strategies, which introduce wireless communication modules in the voltage/current closed loop [16], [17], [19], [28], the reliability of the WPTS can be improved significantly.

VI. EXPERIMENTAL EVALUATION

A. Experimental Prototype

To verify the previous analysis, a 500-W experimental prototype is built up, which is shown in Fig. 19. The prototype includes a dc source (IT6525 C), a high-frequency inverter, an SS resonant network, a full-bridge AR, and an electronic load (IT8814B). Energy is transferred from the dc source to the electronic load. The primary inverter and the secondary AR are controlled by two control boards based on DSP28335, respectively. The MOSFETs used in the inverter and the AR are IXTQ96N20Ps. The primary and secondary controllers exchange information by the wireless communication modules (RF2.4 G). The coupled coils are made by Litz wire. The structure of windings is carefully designed to reduce ESRs and to increase coupling coefficient. The waveforms are recorded by the oscilloscope (Tektronix MDO4104 C) and the overall system efficiency is measured by the power analyzer (HIOKI 3390). Detailed experimental parameters are listed in Table IV.

B. Operating Waveforms of JC-VZA

1) Steady-State Experimental Results: To verify the validity of the proposed JC-VZA, the operating waveforms of the WPTS

TABLE IV
PARAMETERS OF THE WPTS

Symbol	Quantity	Value
L_1	primary resonant inductor	118.43μH
C_1	primary resonant capacitor	29.92nF
f_1	primary resonant frequency	84.55kHz
R_1	primary ESR of resonant network	0.12Ω
L_2	secondary resonant inductor	118.55μH
C_2	secondary resonant capacitor	29.88nF
f_2	secondary resonant frequency	84.56kHz
R_2	secondary ESR of resonant network	0.12Ω
R_{dson}	on-time drain-to-source resistance of IXTQ96N20Ps	0.024Ω
N_1, N_2	number of turns	15
R_{L}	load resistor	8Ω-200Ω
d	face to face distance of coils	12.5cm-20.5cm
k	coupling coefficient	0.20-0.10
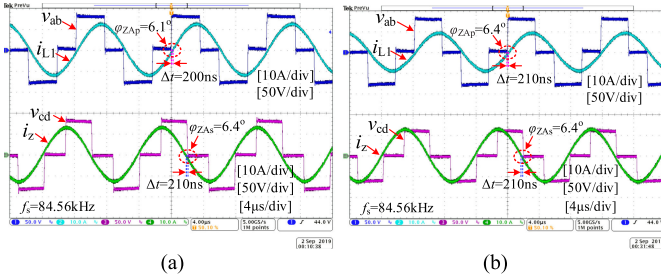
Fig. 20. Operating waveforms for the required output voltage with JC-VZA, when φ^*_{ZAp} and φ^*_{ZAs} are set to 6°. (a) $V_1 = 80$ V, $V_2 = 80$ V, $K_{\mathrm{cv}} = 1$, $k = 0.1$, $R_{\mathrm{L}} = 20$ Ω, and $P_{\mathrm{u}} = 0.388$. (b) $V_1 = 80$ V, $V_2 = 60$ V, $K_{\mathrm{cv}} = 0.75$, $k = 0.1$, $R_{\mathrm{L}} = 15$ Ω, and $P_{\mathrm{u}} = 0.388$.

Fig. 21. Operating waveforms for the required output voltage with JC-VZA, when φ^*_{ZAp} is set to 6° and φ^*_{ZAs} is set as different values. (a) φ^*_{ZAs} is set to 55°, when $V_1 = 80$ V, $V_2 = 30$ V, $K_{\mathrm{cv}} = 0.375$, $k = 0.1$, $R_{\mathrm{L}} = 10$ Ω, and $P_{\mathrm{u}} = 0.291$. (b) φ^*_{ZAs} is set to 30°, when $V_1 = 80$ V, $V_2 = 30$ V, $K_{\mathrm{cv}} = 0.375$, $k = 0.1$, $R_{\mathrm{L}} = 20$ Ω, and $P_{\mathrm{u}} = 0.146$.
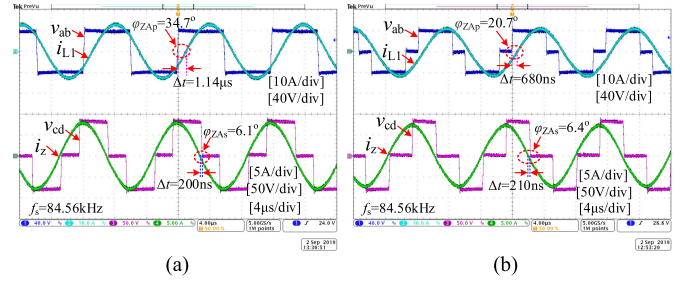
Fig. 22. Operating waveforms for the required output voltage with JC-VZA, when φ^*_{ZAs} is set to 6° and φ^*_{ZAp} is set as different values. (a) φ^*_{ZAp} is set to 35°, when $V_1 = 40$ V, $V_2 = 80$ V, $K_{\mathrm{cv}} = 2$, $k = 0.1$, $R_{\mathrm{L}} = 26.7$ Ω, and $P_{\mathrm{u}} = 0.583$. (b) φ^*_{ZAp} is set to 20°, when $V_1 = 40$ V, $V_2 = 80$ V, $K_{\mathrm{cv}} = 2$, $k = 0.1$, $R_{\mathrm{L}} = 40$ Ω, and $P_{\mathrm{u}} = 0.388$.
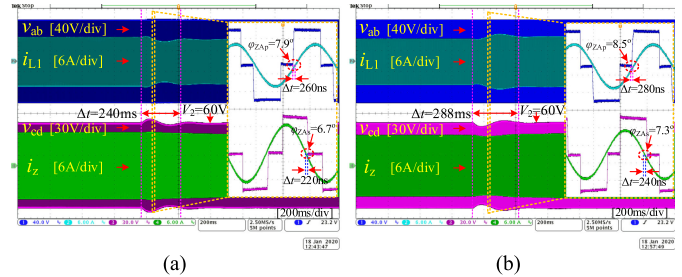
Fig. 23. Dynamic waveforms with the step change of R_{L}, when $V_1 = 80$ V, $V_2 = 60$ V, $k = 0.15$, $\varphi^*_{\mathrm{ZAp}} = 6°$, and $\varphi^*_{\mathrm{ZAs}} = 6°$. (a) Changing R_{L} from 15 to 20 Ω. (b) Changing R_{L} from 20 to 15 Ω.

are shown as follows. When the WPTS operates in Case III, the instructions of ZVS angles (φ^*_{ZAp} and φ^*_{ZAs}) should be set as 0° to make the WPTS operate at the point O. V_1 is set to 80 V, while V_2 is controlled as 80 and 60 V, respectively. The steady-state operating waveforms of the WPTS are shown in Fig. 20. Due to the deadtime effect, φ^*_{ZAp} and φ^*_{ZAs} should be set slightly larger than 0° to make the system achieve ZVS completely. Here, φ^*_{ZAp} and φ^*_{ZAs} are set to 6°. Experimental results show that φ_{ZAp} and φ_{ZAs} are close to 6°, which verify the effectiveness of JC-VZA very well.

When the WPTS operates in Cases I and II, φ^*_{ZAp} should be set to 0° while φ^*_{ZAs} should be adjusted to achieve the minimum power loss. Here, V_1 is set to 80 V, while V_2 is controlled as 30 V with different R_{L}. The steady-state operating waveforms of the WPTS are shown in Fig. 21. Here, φ^*_{ZAp} is set to 6°, while φ^*_{ZAs} is set to 55° or 30°, respectively. Experimental results show that φ_{ZAp} is closed to 6° while φ_{ZAs} is 54.8° or 30.1°, respectively, which perfectly verify the effectiveness of JC-VZA.

When the WPTS operates in Cases IV and V, φ^*_{ZAs} should be set to 0° while φ^*_{ZAp} should be adjusted to achieve the minimum power loss. Here, V_1 is set to 40 V, while V_2 is controlled as 80 V with different R_{L}. The steady-state operating waveforms of the WPTS are shown in Fig. 22. Here, φ^*_{ZAs} is set to 6°, while φ^*_{ZAp} is set to 35° or 20°, respectively. Experimental results show that φ_{ZAs} is close to 6° while φ_{ZAp} is 34.7° or 20.7°, respectively, which also perfectly verify the effectiveness of JC-VZA.

2) Dynamic Performances: To verify the stability of the proposed JC-VZA, the dynamic performances are presented with the step change of the load resistor R_{L}. Fig. 23 presents the dynamic responses by the step change of R_{L} between 15 and 20 Ω while V_2, φ_{ZAp}, and φ_{ZAs} are kept constant. The dynamic setting times are 240 and 288 ms, respectively. The experimental results verify that the WPTS with the proposed JC-VZA can not only achieve ZVS of all switches, but also obtain the perfect performances of anti-load disturbance.

Moreover, when both φ^*_{ZAp} and φ^*_{ZAs} are set to 10°, the starting and shutdown processes of the WPTS with JC-VZA are also presented in Fig. 24. Fig. 24(a) shows the starting process, where the input dc voltage V_1 increases linearly from 0 V and reaches
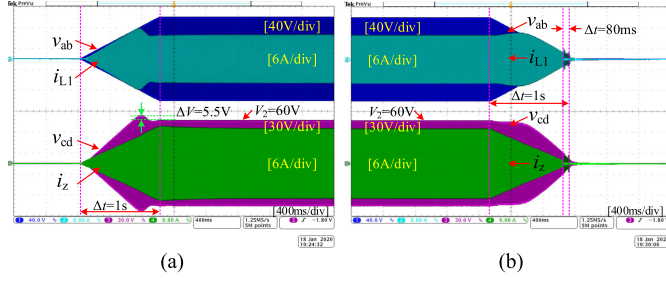
Fig. 24.   Starting and shutdown processes of the WPTS with the proposed JC-VZA, when $V_1 = 80$ V, $V_2 = 60$ V, $k = 0.15$, $R_\mathrm{L} = 15$ Ω, $\varphi_{\mathrm{ZAp}}^* = 10°$, and $\varphi_{\mathrm{ZAs}}^* = 10°$. (a) In the starting process. (b) In the shutdown process.
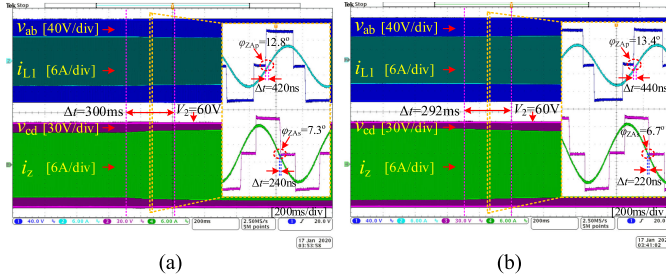
Fig. 25.   Dynamic waveforms with the step change of φ_{ZAp}, when $V_1 = 80$ V, $V_2 = 60$ V, $k = 0.15$, $R_\mathrm{L} = 15$ Ω, and $\varphi_{\mathrm{ZAs}}^* = 6°$. (a) Changing φ_{ZAp}^* from 6° to 16°. (b) Changing φ_{ZAp}^* from 16° to 6°.

80 V within 1 s. Then, the secondary resonant current i_z gradually increases almost linearly without any oscillation. However, the output dc voltage V_2 gradually increases with a small overshoot ($< 10\%$). Subsequently, Fig. 24(b) presents the corresponding shutdown process of the WPTS, where V_1 decreases linearly from 80 V and reaches 0 V within 1 s. In this process, both i_z and v_{cd} merely have overshoots in the vast majority of time duration of shutdown. By the way, in the last 80 ms, there are some oscillations because "Pulse Losing" of driver pulses [16] caused by too small resonant current happens in the AR, which barely has an impact on the safe operation of the system. In a word, the experimental results verify that the WPTS with the proposed JC-VZA also obtains perfect dynamic performances in the starting and shutdown processes, which also demonstrates its unparalleled superiority and excellent applicability.

C. Selection of Time Interval

As demonstrated in Section V-C, to avoid the oscillations in the WPTS and improve the stability of the JC-VZA for dynamic efficiency optimization, the appropriate time interval for exchanging the information of two sides should be selected. Here, $t_{\mathrm{s}1}$ or $t_{\mathrm{s}2}$ is measured accurately by the step changes of φ_{ZAp}^* or φ_{ZAs}^* in the experiments, respectively. On the one hand, the dynamic waveforms with the step changes of φ_{ZAp}^* and a constant φ_{ZAs}^* are shown in Fig. 25. The dynamic setting times are 300 and 292 ms, respectively. On the other hand, the dynamic waveforms with the step changes of φ_{ZAs}^* and a constant φ_{ZAp}^* are shown in Fig. 26. The dynamic setting times are 168 and 172 ms, respectively. Therefore, $t_{\mathrm{s}1} = 300$ ms and $t_{\mathrm{s}2} = 172$ ms. According to (54) and (55), Δt is set to 28 ms in consideration of
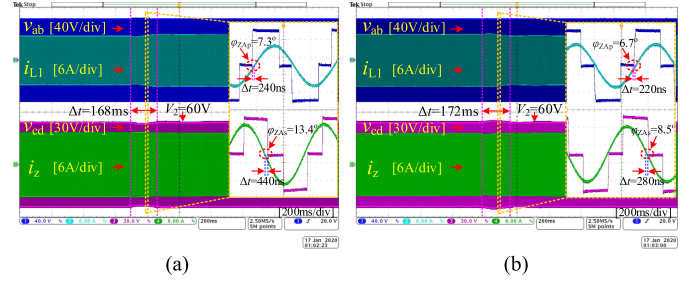
Fig. 26.   Dynamic waveforms with the step change of φ_{ZAs}, when $V_1 = 80$ V, $V_2 = 60$ V, $k = 0.15$, $R_\mathrm{L} = 15$ Ω, and $\varphi_{\mathrm{ZAp}}^* = 6°$. (a) Changing φ_{ZAs}^* from 6° to 16°. (b) Changing φ_{ZAs}^* from 16° to 6°.

a certain time margin. Therefore, the highest frequency for exchanging the information of two sides, f_{exc}, is $1/500$ ms $= 2$ Hz.

D. Verification of Power Losses

Similar to the verifications in Section IV-C, the conclusions in Table II need to be validated by experiments. With the parameters listed in Table IV, P_{res}' on the boundary curves AOB is measured and compared with the calculation results. Based on the five cases listed in Table II, the corresponding comparison results are shown in Figs. 27–29.

1) Case III: If $1/\sqrt{2} \le K_{\mathrm{cv}} \le \sqrt{2}$, the operating conditions in Case III are set as three situations: $K_{\mathrm{cv}} = 1$, 0.75, and 1.33, respectively. With the parameters listed in Table IV, the theoretical calculations and experimental results of P_{res}' on the boundary curves AOB are carried out and compared, which are plotted in Fig. 27. It shows that the experimental results have a good agreement with the calculated ones. Based on the variation tendency of P_{res}' on the boundary curves AOB, the WPTS will achieve the minimum power loss near the point O, which is conform to the conclusions of Case III in Table II.

2) Case I and Case II: If $K_{\mathrm{cv}} < 1/\sqrt{2}$, the operating conditions in Case I and Case II are set as two situations: $P_{\mathrm{u}} = 0.291$, $K_{\mathrm{cv}} = 0.375$, and $P_{\mathrm{u}} = 0.146$, $K_{\mathrm{cv}} = 0.375$. With the parameters listed in Table IV, the theoretical calculations and experimental results of P_{res}' on the boundary curves AOB are also carried out and compared, which are plotted in Fig. 28.

Since $K_{\mathrm{cv}} = 0.375 < 1/\sqrt{2}$ and $P_{\mathrm{u}} = 0.291 > 0.281 = P_{\mathrm{uc}1}$, the WPTS will achieve the minimum power loss when φ_{ZAs} is set to its maximum value and φ_{ZAp} is set to 0° according to the conclusions of Case I in Table II. In Fig. 28(a), the theoretical calculation results conform to the conclusions of Case I in Table II, while the experimental results have slight differences. In Fig. 28(a), P_{res}' is the monotonic increasing function of φ_{ZAp} when $\varphi_{\mathrm{ZAs}} = 0°$ in the right-hand side. In the left-hand side, if φ_{ZAs} is close to 0°, P_{res}' gradually decreases as φ_{ZAs} gradually increases when $\varphi_{\mathrm{ZAp}} = 0°$. However, if φ_{ZAs} keeps away from 0°, P_{res}' has a subtle increase. The basic reason is that the decline of P_{res}' is not distinct as φ_{ZAs} increases when φ_{ZAs} approaches its maximum value. Meanwhile, the turn-off loss increases slowly as φ_{ZAs} gradually increases. Therefore, the total power loss of the WPTS presents a subtle increase when φ_{ZAs} keeps away from 0°. Anyhow, there will be a minimum
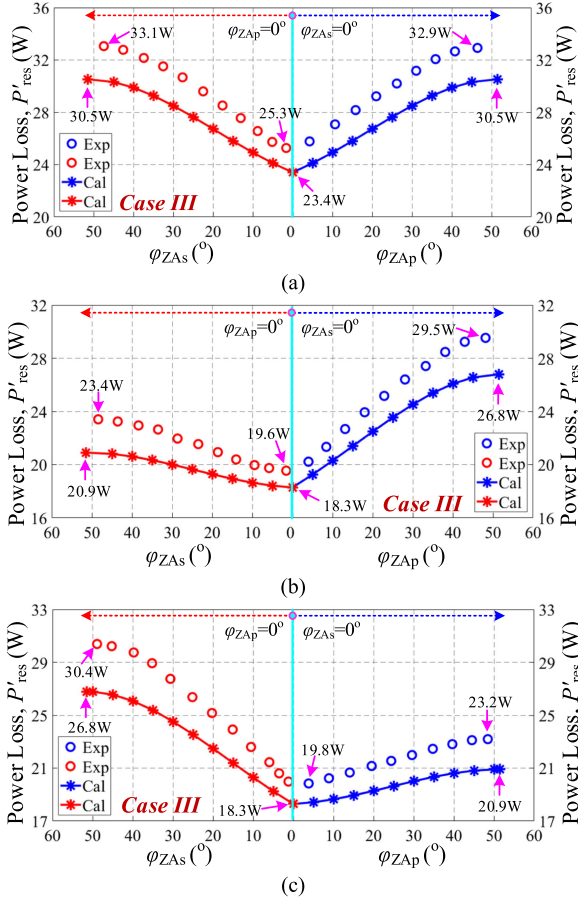
Fig. 27. Comparisons of P'_{res} between theoretical calculations and experimental measurements when $k = 0.1$. (a) $V_1 = 80$ V, $V_2 = 80$ V, $I_2 = 4$ A, $R_L = 20$ Ω, $K_{\text{cv}} = 1$, and $P_u = 0.388$. (b) $V_1 = 80$ V, $V_2 = 60$ V, $I_2 = 4$ A, $R_L = 15$ Ω, $K_{\text{cv}} = 0.75$, and $P_u = 0.388$. (c) $V_1 = 60$ V, $V_2 = 80$ V, $I_2 = 3$ A, $R_L = 26.7$ Ω, $K_{\text{cv}} = 1.33$, and $P_u = 0.388$.

Fig. 28. Comparisons of P'_{res} between theoretical calculations and experimental measurements when $k = 0.1$. (a) $V_1 = 80$ V, $V_2 = 30$ V, $I_2 = 3$ A, $R_L = 10$ Ω, $K_{\text{cv}} = 0.375$, and $P_u = 0.291$. (b) $V_1 = 80$ V, $V_2 = 30$ V, $I_2 = 1.5$ A, $R_L = 20$ Ω, $K_{\text{cv}} = 0.375$, and $P_u = 0.146$.
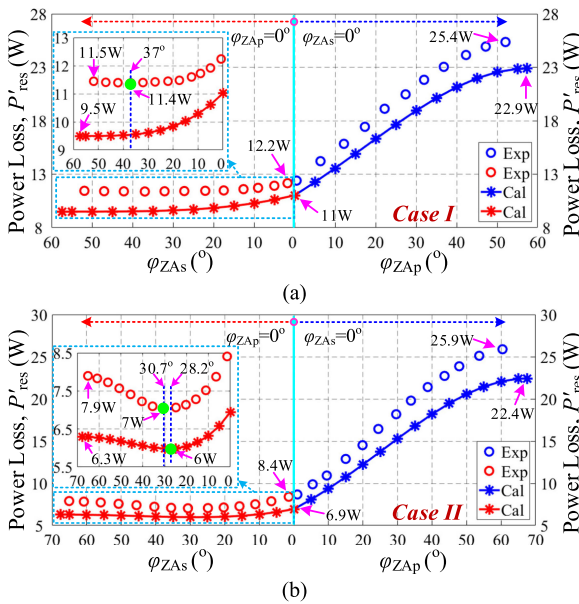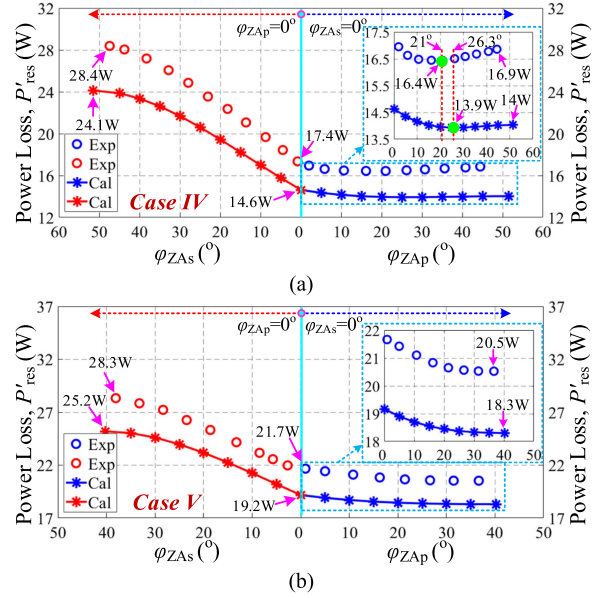

Fig. 29. Comparisons of P'_{res} between theoretical calculations and experimental measurements when $k = 0.1$. (a) $V_1 = 40$ V, $V_2 = 80$ V, $I_2 = 2$ A, $R_L = 40$ Ω, $K_{\text{cv}} = 2$, and $P_u = 0.388$. (b) $V_1 = 40$ V, $V_2 = 80$ V, $I_2 = 3$ A, $R_L = 26.7$ Ω, $K_{\text{cv}} = 2$, and $P_u = 0.583$.

power loss in the left-hand side, which can be easily found by the dynamic efficiency optimization method based on P&O.

In Fig. 28(b), P'_{res} is the single-valley function of φ_{ZAs} when $\varphi_{\text{ZAp}} = 0°$ and the monotonic increasing function of φ_{ZAp} when $\varphi_{\text{ZAs}} = 0°$. Therefore, the WPTS achieves the minimum power loss at the valley value, which is on the trajectory OA. Since $K_{\text{cv}} = 0.375 < 1/\sqrt{2}$ and $P_u = 0.146 < 0.281 = P_{\text{uc1}}$, the conclusions of Case II in Table II are also verified very well.

3) Case IV and Case V: When $K_{\text{cv}} > \sqrt{2}$, the operating conditions in Case IV and Case V are set as two situations: $P_u = 0.388$, $K_{\text{cv}} = 2$ and $P_u = 0.583$, $K_{\text{cv}} = 2$. With the parameters listed in Table IV, the theoretical calculations and experimental results of P'_{res} on the boundary curves AOB are also carried out and compared, which are plotted in Fig. 29. It shows that the experimental results have a good agreement with the calculated ones.

In Fig. 29(a), P'_{res} is the monotonic increasing function of φ_{ZAs} when $\varphi_{\text{ZAp}} = 0°$ and the single-valley function of φ_{ZAp} when $\varphi_{\text{ZAs}} = 0°$. Therefore, the WPTS will achieve the minimum power loss at the valley value, which is on the trajectory OB. Since $K_{\text{cv}} = 2 > \sqrt{2}$ and $P_u = 0.388 < 0.5 = P_{\text{uc2}}$, the conclusions of Case IV in Table II are validated very well.

In Fig. 29(b), P'_{res} is the monotonic increasing function of φ_{ZAs} when $\varphi_{\text{ZAp}} = 0°$ and the monotonic decreasing function of φ_{ZAp} when $\varphi_{\text{ZAs}} = 0°$. Therefore, the WPTS will achieve the minimum power loss near the point B. Since $K_{\text{cv}} = 2 > \sqrt{2}$ and $P_u = 0.583 > 0.5 = P_{\text{uc2}}$, the conclusion of Case V in Table II are also validated very well.

E. Comparisons of Power Loss and Efficiency

1) Comparisons of Typical Operating Points: To emphasize the importance in selecting the appropriate operating point with

TABLE V
OPERATING CONDITIONS AND CORRESPONDING MINIMUM POWER LOSSES

Case	K_{cv}	Point A (W)	Point O (W)	Point B (W)	P_{res_opt} (W)	R_d of Point A (%)	R_d of Point O (%)	R_d of Point B (%)	Transfer Power (W)	System efficiency (%)
I	0.375	11.5	12.2	25.4	11.4	0.87	6.56	55.12	90	88.8
II	0.375	7.9	8.4	25.9	7.0	11.39	16.67	72.97	45	86.5
	1.0	33.1	25.3	32.9	25.3	23.56	/	23.10	320	92.7
III	0.75	23.4	19.6	29.5	19.6	16.24	/	33.56	240	92.4
	1.33	30.4	19.8	23.2	19.8	34.87	/	14.66	240	92.4
IV	2.0	28.4	17.4	16.9	16.4	42.25	5.75	2.96	160	90.7
V	2.0	28.3	21.7	20.5	20.5	27.53	5.26	/	240	92.1

the proposed JC-VZA, the comparisons of P'_{res} between three typical operating points (point A, O, B) and the minimum power loss point are made. Here, we define the rate of decreasing power loss as

$$R_d = (P'_{res} - P_{res\_opt})/P'_{res} \times 100\% \qquad (56)$$

where P_{res_opt} is the minimum power loss in one case.

Under the same operating conditions, the rates of decreasing power loss in three typical points are calculated and shown in Table V. Compared with other operating points, the minimum power loss point can decrease the system power loss tremendously. Therefore, it is significant to find out and operate at the minimum power loss point, which is vital for improving the system transfer efficiency.

2) Compared With Impedance Matching Method: Many researchers insist that the impedance matching method can maximize the transfer efficiency by minimizing the power loss of the resonant network. As stated previously, to achieve impedance matching, auxiliary dc–dc converters commonly need to be added, which will induce extra power loss and increase extra cost. To save extra dc–dc converters and money, the AR is recently used to achieve the impedance matching [16]–[19], which can indeed save extra dc–dc converters and improve the transfer efficiency. However, ZVS of all switches in the WPTS cannot be achieved completely, which induces a relatively large power loss and decreases the overall transfer efficiency.

To be honest, with the proposed JC-VZA, the resonant current will increase to some extent because the reactive power is introduced in the AR. However, by using the proposed JC-VZA for dynamic efficiency optimization, the introduced reactive power can be selected reasonably to achieve the minimum total power loss under ZVS conditions, and the resonant current will not increase too much consequently. On the contrary, it is by introducing necessary reactive power in the AR that all the switches of the WPTS can achieve ZVS completely. That is the most outstanding advantage of the proposed JC-VZA with dynamic efficiency optimization method.

By using the traditional DPSC, the system charging power and transfer efficiency versus R_L are shown in Fig. 30 with blue lines when the system achieves the impedance matching and CC/CV charging simultaneously. Moreover, the same charging process has been conducted by using the proposed JC-VZA for dynamic efficiency optimization and the corresponding charging efficiencies are also plotted in Fig. 30 with red lines. In Fig. 30, with a coupling coefficient k of 0.2 or 0.15, compared with the benchmark WPTS that uses DPSC and impedance
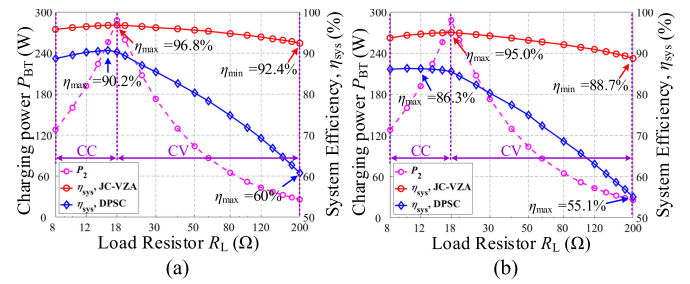

Fig. 30. Charging experiments simulated by a sliding rheostat with the proposed JC-VZA and DPSC when (a) $k = 0.2$ and (b) $k = 0.15$.

matching technique, our system achieves a 6.6% or 8.7% efficiency improvement under rated power as well as a 32.4% or 33.6% improvement under the light-load condition, respectively. Therefore, the experimental results powerfully verify that it is vital to introduce appropriate reactive power in the WPTS to make all switches achieve ZVS, which is very important to increase the system transfer efficiency. In practice, the proposed JC-VZA for dynamic efficiency optimization is a very effective method to select the appropriate reactive power by controlling ZVS angles of both sides in a certain operating condition.

3) Compared With Other Reported WPTSs: To compare this work with other representative reported WPTSs concerning the transfer efficiency more reasonably, the resonant frequency should be limited below 1 MHz and the transfer power should be limited below 1 kW. The system transfer efficiencies in some other published papers are summarized in Table VI. The key parameters, including coil diameter, transfer distance, coupling coefficient, transfer power, and system efficiency are listed in this table. Taking the coil size and the transfer distance into account, a normalized distance D_{nom} is defined as the transfer distance over the coil diameter [20], [29], [30], which is

$$D_{nom} = d \Big/ \sqrt{D_1 \times D_2} \qquad (57)$$

where D_1 and D_2 are the diameters of the primary and secondary coils, respectively. The normalized distance is considered because it is the major limiting factor on the transfer efficiency. Fig. 31 shows the system transfer efficiency with respect to the normalized distance.

In Fig. 31, it can be seen that when the normalized distance is larger, the lower efficiency can be achieved for all WPTSs. The prototype in this article can achieve higher efficiency at the same normalized distance, and provide larger normalized distance for the same efficiency.

TABLE VI
PERFORMANCE COMPARISONS OF REPORTED WPTSs

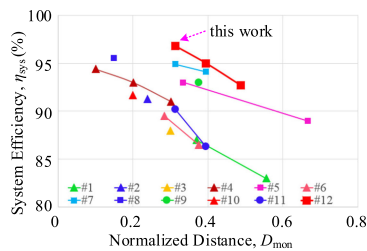| #	Paper reference	Operating Frequency (kHz)	Tx Coil Size (mm)	Rx Coil Size (mm)	Distance d (mm)	Normalized Distance	Coupling Coefficient	Transfer Power P_o(W)	Efficiency (%)
1	[15]	515	270	270	100	0.37	0.18	25	87
					150	0.56	0.1	25	83
2	[31]	85	420	420	100	0.24	0.13	~1000	91.3
3	[32]	100	>200	>200	60	0.3	0.277	200	88
					76	0.1	0.5	200	94.4
4	[33]	150	760	760	152	0.2	0.3	500	93
					229	0.3	0.25	1000	91
5	[29]	909	300	300	100	0.33	0.23	10	93
					200	0.67	0.08	10	89
6	[34]	200	88	88	25	0.28	0.25	90	89.5
					33	0.38	0.17	90	86.5
7	[20]	90~110	400	400	125	0.31	0.2	288	94.9
					158	0.4	0.15	288	94.1
8	[35]	85	800	800	120	0.15	0.31	900	95.5
9	[18]	85	400	400	150	0.38	0.22	1000	93
10	[19]	30	500	500	100	0.2	0.186	800	91.7
11	[16]	85	400	400	125	0.31	0.2	288	90.2
					158	0.4	0.15	288	86.3
12	This work	85	400	400	125	0.31	0.2	288	96.8
					158	0.4	0.15	288	95.0
					190	0.5	0.1	288	92.7

Fig. 31. Efficiency comparisons of WPTSs listed in Table VI.

VII. CONCLUSION

This article has developed a very high-efficiency WPTS that simultaneously achieves tight voltage regulation and ZVS of all switches without any additional dc–dc converter. It features a novel JC-VZA that automatically finds the highest system efficiency point under ZVS conditions. This high-efficiency point is calculated through a detailed power loss analysis. Experimental results clearly demonstrate that our WPTS can successfully achieve the impressively high efficiency in a wide range. Specifically, with a coupling coefficient k of 0.2 or 0.15, the maximum system efficiency reaches 96.8% or 95.0%, respectively, under the rated-load condition (i.e., 288 W). Notably, the efficiency remains as high as 92.4% or 88.7% under a 9% light-load condition (i.e., 26 W, 9% of 288 W). Compared with the benchmark WPTS that uses DPSC and impedance matching technique, our system achieves a 6.6% or 8.7% efficiency improvement under rated power as well as a 32.4% or 33.6% improvement under the light-load condition, respectively.

REFERENCES

[1] C. Liu, C. Jiang, J. Song, and K. T. Chau, "An effective sandwiched wireless power transfer system for charging implantable cardiac pacemaker," *IEEE Trans. Ind. Electron.*, vol. 66, no. 5, pp. 4108–4117, May 2019.

[2] M. R. Basar, M. Y. Ahmad, J. Cho, and F. Ibrahim, "An improved wearable resonant wireless power transfer system for biomedical capsule endoscope," *IEEE Trans. Ind. Electron.*, vol. 65, no. 10, pp. 7772–7781, Oct. 2018.

[3] M. R. Basar, M. Y. Ahmad, J. Cho, and F. Ibrahim, "Stable and high-efficiency wireless power transfer system for robotic capsule using a modified helmholtz coil," *IEEE Trans. Ind. Electron.*, vol. 64, no. 2, pp. 1113–1122, Feb. 2017.

[4] T. Yeo, D. Kwon, S. Khang, and J. Yu, "Design of maximum efficiency tracking control scheme for closed-loop wireless power charging system employing series resonant tank," *IEEE Trans. Power Electron.*, vol. 32, no. 1, pp. 471–478, Jan. 2017.

[5] P. S. Riehl *et al.*, "Wireless power systems for mobile devices supporting inductive and resonant operating modes," *IEEE Trans. Microw. Theory Techn.*, vol. 63, no. 3, pp. 780–790, Mar. 2015.

[6] M. G. Eftekhar, Z. Ouyang, M. A. E. Andersen, P. B. Andersen, L. A. de S. Ribeiro, and E. Schaltz, "Efficiency study of vertical distance variations in wireless power transfer for e-mobility," *IEEE Trans. Magn.*, vol. 52, no. 7, Jul. 2016, Art. no. 8401004.

[7] Z. Yan *et al.*, "Frequency optimization of a loosely coupled underwater wireless power transfer system considering eddy current loss," *IEEE Trans. Ind. Electron.*, vol. 66, no. 5, pp. 3468–3476, May 2019.

[8] T. Orekan, P. Zhang, and C. Shih, "Analysis, design, and maximum power-efficiency tracking for undersea wireless power transfer," *IEEE J. Emerg. Sel. Topics Power Electron.*, vol. 6, no. 2, pp. 843–854, Jun. 2018.

[9] K. Zhang, Y. Ma, Z. Yan, Z. Di, B. Song, and A. P. Hu, "Eddy current loss and detuning effect of seawater on wireless power transfer," *IEEE J. Emerg. Sel. Topics Power Electron.*, vol. 8, no. 1, pp. 909–917, Mar. 2020.

[10] T. Kan, T. Nguyen, J. C. White, R. K. Malhan, and C. C. Mi, "A new integration method for an electric vehicle wireless charging system using LCC compensation topology: Analysis and design," *IEEE Trans. Power Electron.*, vol. 32, no. 2, pp. 1638–1650, Feb. 2017.

[11] F. Lu, H. Zhang, H. Hofmann, W. Su, and C. C. Mi, "A dual-coupled LCC-compensated IPT system with a compact magnetic coupler," *IEEE Trans. Power Electron.*, vol. 33, no. 7, pp. 6391–6402, Jul. 2018.

[12] S. Li and C. C. Mi, "Wireless power transfer for electric vehicle applications," *IEEE J. Emerg. Sel. Topics Power Electron.*, vol. 3, no. 1, pp. 4–17, Mar. 2015.

[13] S. Li, W. Li, J. Deng, T. D. Nguyen, and C. C. Mi, "A double-sided LCC compensation network and its tuning method for wireless power transfer," *IEEE Trans. Veh. Technol.*, vol. 64, no. 6, pp. 2261–2273, Jun. 2015.

[14] G. Buja, M. Bertoluzzo, and K. N. Mude, "Design and experimentation of WPT charger for electric city car," *IEEE Trans. Ind. Electron.*, vol. 62, no. 12, pp. 7436–7447, Dec. 2015.

[15] H. Li, J. Li, K. Wang, W. Chen, and X. Yang, "A maximum efficiency point tracking control scheme for wireless power transfer systems using magnetic resonant coupling," *IEEE Trans. Power Electron.*, vol. 30, no. 7, pp. 3998–4008, Jul. 2015.

[16] Y. Jiang et al., "Phase-locked loop combined with chained trigger mode used for impedance matching in wireless high power transfer," *IEEE Trans. Power Electron.*, vol. 35, no. 4, pp. 4272–4285, Apr. 2020.

[17] B. X. Nguyen et al., "An efficiency optimization scheme for bidirectional inductive power transfer systems," *IEEE Trans. Power Electron.*, vol. 30, no. 11, pp. 6310–6319, Nov. 2015.

[18] Y. Li, J. Hu, F. Chen, Z. Li, Z. He, and R. Mai, "Dual-phase-shift control scheme with current-stress and efficiency optimization for wireless power transfer systems," *IEEE Trans. Circuits Syst. I, Reg. Papers*, vol. 65, no. 9, pp. 3110–3121, Sep. 2018.

[19] R. Mai, Y. Liu, Y. Li, P. Yue, G. Cao, and Z. He, "An active-rectifier-based maximum efficiency tracking method using an additional measurement coil for wireless power transfer," *IEEE Trans. Power Electron.*, vol. 33, no. 1, pp. 716–728, Jan. 2018.

[20] Y. Jiang, L. Wang, Y. Wang, J. Liu, M. Wu, and G. Ning, "Analysis, design, and implementation of WPT system for EV's battery charging based on optimal operation frequency range," *IEEE Trans. Power Electron.*, vol. 34, no. 7, pp. 6890–6905, Jul. 2019.

[21] Y. Jiang, L. Wang, Y. Wang, J. Liu, X. Li, and G. Ning, "Analysis, design, and implementation of accurate ZVS angle control for EV battery charging in wireless high-power transfer," *IEEE Trans. Ind. Electron.*, vol. 66, no. 5, pp. 4075–4085, May 2019.

[22] X. Zhang et al., "A control strategy for efficiency optimization and wide zvs operation range in bidirectional inductive power transfer system," *IEEE Trans. Ind. Electron.*, vol. 66, no. 8, pp. 5958–5969, Aug. 2019.

[23] F. Liu, W. Lei, T. Wang, C. Nie, and Y. Wang, "A phase-shift soft-switching control strategy for dual active wireless power transfer system," in *Proc. IEEE Energy Convers. Congr. Expo.*, 2017, pp. 2573–2578.

[24] H. Li, K. Wang, J. Fang, and Y. Tang, "Pulse density modulated ZVS full-bridge converters for wireless power transfer systems," *IEEE Trans. Power Electron.*, vol. 34, no. 1, pp. 369–377, Jan. 2019.

[25] Y. P. Chan, K. H. Loo, M. Yaqoob, and Y. M. Lai, "A structurally reconfigurable resonant dual-active-bridge converter and modulation method to achieve full-range soft-switching and enhanced light-load efficiency," *IEEE Trans. Power Electron.*, vol. 34, no. 5, pp. 4195–4207, May 2019.

[26] J. Everts, "Closed-form solution for efficient ZVS modulation of dab converters," *IEEE Trans. Power Electron.*, vol. 32, no. 10, pp. 7561–7576, Oct. 2017.

[27] F. Krismer and J. W. Kolar, "Closed form solution for minimum conduction loss modulation of dab converters," *IEEE Trans. Power Electron.*, vol. 27, no. 1, pp. 174–188, Jan. 2012.

[28] Y. Yang, W. Zhong, S. Kiratipongvoot, S. Tan, and S. Y. R. Hui, "Dynamic improvement of series - series compensated wireless power transfer systems using discrete sliding mode control," *IEEE Trans. Power Electron.*, vol. 33, no. 7, pp. 6351–6360, Jul. 2018.

[29] H. Li, K. Wang, J. Fang, and Y. Tang, "Pulse density modulated ZVS full-bridge converters for wireless power transfer systems," *IEEE Trans. Power Electron.*, vol. 34, no. 1, pp. 369–377, Jan. 2019.

[30] D. Ahn, S. Kim, J. Moon, and I. Cho, "Wireless power transfer with automatic feedback control of load resistance transformation," *IEEE Trans. Power Electron.*, vol. 31, no. 11, pp. 7876–7886, Nov. 2016.

[31] A. Kamineni, G. A. Covic, and J. T. Boys, "Analysis of coplanar intermediate coil structures in inductive power transfer systems," *IEEE Trans. Power Electron.*, vol. 30, no. 11, pp. 6141–6154, 2015.

[32] Y. H. Sohn, B. H. Choi, E. S. Lee, G. C. Lim, G. Cho, and C. T. Rim, "General unified analyses of two-capacitor inductive power transfer systems: Equivalence of current-source ss and sp compensations," *IEEE Trans. Power Electron.*, vol. 30, no. 11, pp. 6030–6045, 2015.

[33] K. Colak, E. Asa, M. Bojarski, D. Czarkowski, and O. C. Onar, "A novel phase-shift control of semibridgeless active rectifier for wireless power transfer," *IEEE Trans. Power Electron.*, vol. 30, no. 11, pp. 6288–6297, 2015.

[34] Z. Huang, S. Wong, and C. K. Tse, "Control design for optimizing efficiency in inductive power transfer systems," *IEEE Trans. Power Electron.*, vol. 33, no. 5, pp. 4523–4534, 2018.

[35] Y. Tang, Y. Chen, U. K. Madawala, D. J. Thrimawithana, and H. Ma, "A new controller for bidirectional wireless power transfer systems," *IEEE Trans. Power Electroni.*, vol. 33, no. 10, pp. 9076–9087, 2018.

Yongbin Jiang (Student Member, IEEE) was born in Jiangsu, China, in 1990. He received the B.S. degree in electrical automatization from Jiangsu University, Jiangsu, China, in 2012, and the M.S. degree in instrument science and technology from Xi'an Jiaotong University, Xi'an, China, in 2016. He is currently working toward the Ph.D. degree in electrical engineering in Xi'an Jiaotong University, Xi'an, China.

His research interests include wireless power transfer, high frequency, and high power density dc–dc converters, signal processing, and digital control technology.

Dr. Jiang was a recipient of the Best Paper Award of IEEE 10th International Symposium on Power Electronics for Distributed Generation Systems (PEDG) in 2019. He has published one ESI highly cited paper.

Laili Wang (Senior Member, IEEE) was born in Shaanxi province, China, in 1982. He received the B.S., M.S., and Ph.D. degrees in electrical engineering from Xi'an Jiaotong University, Xi'an, China, in 2004, 2007, and 2011, respectively.

Since 2011, he has been a Postdoctoral Research Fellow with the Department of Electrical Engineering, Queen's University, Kingston, ON, Canada. From 2014 to 2017, he was an Electrical Engineer with Sumida, Canada. In 2017, he joined Xi'an Jiaotong University as a Professor. His research interests include package and integration of passive devices in high-frequency high power density dc–dc converters, wireless power transfer, and energy harvesting.

Jingyang Fang (Member, IEEE) received the B.Sc. and M.Sc. degrees in electrical engineering from Xi'an Jiaotong University, Xi'an, China, in 2013 and 2015, respectively, and the Ph.D. degree from the School of Electrical and Electronic Engineering, Nanyang Technological University, Singapore, in 2019.

From May 2018 to August 2018, he was a Visiting Scholar with the Institute of Energy Technology, Aalborg University, Aalborg, Denmark. From August 2018 to August 2019, he was a Research Fellow with the School of Electrical and Electronic Engineering, Nanyang Technological University, Singapore. In August 2019, he joined the Duke University and University of Kaiserslautern, as a Postdoctoral Fellow. His research interests include power quality control, stability analysis and improvement, renewable energy integration, and digital control in more-electronics power systems.

Dr. Fang is the recipient of the Best Paper Award of IEEE Asia Conference on Energy, Power and Transportation Electrification in 2017 and the Best Presenter of IEEE International Power Electronics and Application Conference and Exposition in 2018. He received the Chinese Government Award for Outstanding Self-Financed Students Abroad in 2018 and the Best Thesis Award from NTU in 2019. He has published two ESI highly cited papers.
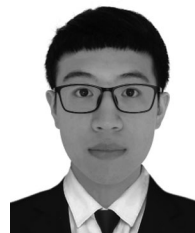
Chenxu Zhao was born in Heilongjiang, China, in 1996. He received the B.S. degree in electrical automatization from Northwestern Polytechnical University, Xi'an, China, in 2019. He is currently working toward the M.S. degree in instrument science and technology with Xi'an Jiaotong University, Xi'an, China.

His research interests include wireless power transfer, high frequency, and high power density dc–dc converters.
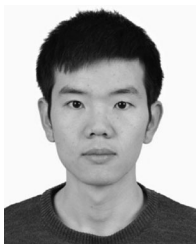
Kangping Wang (Member, IEEE) received the B.S. and Ph.D. degrees in electrical engineering from Xi'an Jiaotong University, Xi'an, China, in 2012 and 2018, respectively.

From August 2016 to August 2017, he was with the Department of ePOWER, Electrical and Computer Engineering, Queen's University, Kingston, ON, Canada, as a Visiting Scholar. Since 2018, he has been an Assistant Researcher with the School of Electrical Engineering, Xi'an Jiaotong University, Xi'an, China. His research interests include high-frequency power converters and wide bandgap devices.

Dr. Wang received the Best Paper Award of the International Conference on Power Electronics–ECCE Asia in 2019.

Yue Wang (Member, IEEE) received the B.S. degree from Xi'an Jiaotong University, Xi'an, China, in 1994, the M.S. degree from Beijing Jiaotong University, Beijing, China, in 2000, and the Ph.D. degree from Xi'an Jiaotong University in 2003, all in electrical engineering.

He is currently a Full Professor with the School of Electrical Engineering, Xi'an Jiaotong University. His research interests include wireless power transfer, active power filters, multilevel converters, and HVDC.